INTERNATIONAL JOURNAL FOR NUMERICAL AND ANALYTICAL METHODS IN GEOMECHANICS
Int. J. Numer. Anal. Meth. Geomech. (2014)
Published online in Wiley Online Library (wileyonlinelibrary.com). DOI: 10.1002/nag.2281

Weak discontinuity in porous media: an enriched EFG method for fully coupled layered porous media

M. Goudarzi and S. Mohammadi*,†

School of Civil Engineering, University of Tehran, Tehran, Iran

SUMMARY

In this paper, a series of multimaterial benchmark problems in saturated and partially saturated two-phase and three-phase deforming porous media are addressed. To solve the process of fluid flow in partially saturated porous media, a fully coupled three-phase formulation is developed on the basis of available experimental relations for updating saturation and permeabilities during the analysis. The well-known element free Galerkin mesh-free method is adopted. The partition of unity property of MLS shape functions allows for the field variables to be extrinsically enriched by appropriate functions that introduce existing discontinuities in the solution field. Enrichment of the main unknowns including solid displacement, water phase pressure, and gas phase pressure are accounted for, and a suitable enrichment strategy for different discontinuity types are discussed. In the case of weak discontinuity, the enrichment technique previously used by Krongauz and Belytschko [*Int. J. Numer. Meth. Engng.*, 1998; 41:1215–1233] is selected. As these functions possess discontinuity in their first derivatives, they can be used for modeling material interfaces, generating only minor oscillations in derivative fields (strain and pressure gradients for multiphase porous media), as opposed to unenriched and constrained mesh-free methods. Different problems of multimaterial poroelasticity including fully saturated, partially saturated one, and two-phase flows under the assumption of fully coupled extended formulation of Biot are examined. As a further development, problems involved with both material interface and impermeable discontinuities, where no fluid exchange is permitted across the discontinuity, are considered and numerically discussed. Copyright © 2014 John Wiley & Sons, Ltd.

Received 7 October 2013; Revised 9 February 2014; Accepted 24 February 2014

KEY WORDS: element-free Galerkin method; multiphase; partially saturated soil; weak discontinuity; fractured porous media; partition of unity enrichment

1. INTRODUCTION

Mechanics of partially saturated porous media is one of the most important branches of mechanics that has gained great attention in the past few decades because of its wide applications in major civil engineering projects. On the basis of the early contributions by Terzaghi [1] and Biot [2], which laid the fundamental concepts of porous media, averaging theories were introduced, and the governing equations for deformable porous systems under nonisothermal multiphase situations were developed and extended to account for various thermodynamic effects [3, 4]. For a comprehensive explanation and discussion on the governing equations and numerical discretization of fully coupled deforming porous media, see [5].

Various numerical solutions to the problem of three phase partially saturated porous media can be found in [6–11], all using the finite element method and assuming different static and dynamic conditions and miscible and nonmiscible fluid phases. Despite the fact that the finite element method is known as a robust and suitable tool for solving general partial differential equations, it suffers from some drawbacks in certain problems that involve severe mesh distortions [12, 13] and general crack propagation problems where remeshing strategies are needed [14]. In addition, in the case of stationary

*Correspondence to: S. Mohammadi, School of Civil Engineering, University of Tehran, Tehran, Iran.
†E-mail: smoham@ut.ac.ir

cracks, a conforming and highly refined mesh is required to capture the singular gradient fields at the tip of discontinuity [15]. Here, an alternative element-free Galerkin method is presented on the basis of the moving least-squares (MLS) shape functions[16–20].

Among the mesh-free methods, Modaressi and Aubert [21] proposed an element free Galerkin (EFG) algorithm for deforming multiphase porous media, in which the displacement of the solid skeleton was modeled by the standard finite element method, whereas fluid pore pressures were modeled using the EFG approach. They also proposed a method for handling material discontinuities based on the Lagrange multipliers. Wang *et al*. [22] developed a mesh-free algorithm based on the consolidation theory of Biot for the problem of one-dimensional saturated porous media. Samimi and Pak [23] used EFG method to solve the problem of saturated porous systems in three dimensions. Khoshghalb and Khalili [24] developed a new time integration scheme with second-order accuracy based on the mesh-free radial point interpolation method (RPIM). They also developed a novel formulation using the same methodology for partially saturated two-phase fluid flow, taking into account the hydraulic hysteresis [25]. Other important contributions in continuous porous media using mesh-free algorithms can be found in [26–30].

On the basis of the basic concepts of generalized finite element method [31] and partition of unity finite element method [32], the local enrichment of finite element solutions for capturing of arbitrarily oriented discontinuities within a domain was proposed by Moes *et al*. [33] and Belytschko and Black [34]. This method, now called the extended finite element method, rectifies the need for remeshing the solution domain during the propagation of discontinuities and does not require conforming the discontinuity lines with element edges [35, 36]. Imposition of arbitrary weak discontinuities was proposed by [33], and modified strategies were exploited [37–41] to correct the poor convergence ratios of original algorithms.

Multiple contributions that employ the extrinsic enrichment strategy to fully coupled porous media exist in the literature. Rethore *et al*. [42] developed a two-scale enriched finite element method formulation around the crack region under the fully saturated state. An extension of the proposed model to cohesive cracks for partially saturated porous media assuming active and passive gas pressures were proposed by [43] and [44], respectively. Irzal *et al*.[45] developed a formulation for cohesive crack propagation in geometrically nonlinear saturated porous media under the framework of extended finite element method (XFEM), whereas Khoei *et al*.[46] proposed an enriched finite element formulation for nonisothermal saturated porous media with impermeable discontinuities.

Simulation of strong discontinuities by the extrinsic enrichment in mesh-free methods has gained great attention in the past few years. A three-dimensional enriched mesh-free method for representing continuous multiple cohesive fractures was developed in [47]. Rabczuk and Belytschko [48, 49] and Rabczuk *et al*. [50] proposed a simplified mesh-free method for arbitrary evolving cracks in which no representation of the crack's topology was required. Application of extrinsically enriched mesh-free methods to modeling slip lines in geological materials with cohesive surfaces was proposed in [51] and the same approach was applied for thin shells in [52, 53] and to fluid-structure interaction in [54]. Here, the partition of unity property of MLS shape functions, proposed in [55–58], is utilized to model the strong discontinuities using the extrinsic enrichment of the basic mesh-free solution.

A challenging problem in enriched mesh-free methods is the problem of material discontinuity, which is discussed in this paper. Such a discontinuity is a result of difference in material properties and causes discontinuity in the first derivatives of the field variables while the main unknowns remain continuous. As many of practical porous applications consist of different soil layers with different material properties, it is of great importance to consider this type of discontinuity. For example, in hydraulic embankments, soils with different values of permeability and stiffness are used or the soil foundations may naturally be consisted of different soil properties. This type of discontinuity, known as the weak discontinuity, can be captured by the finite element method by adjusting the element edges to coincide with the line of discontinuity. In mesh-free methods, however, because of the continuity of derivatives in EFG method, continuous but oscillatory solution for derivatives is obtained, as reported in [19]. There are basically two methods for handling material discontinuities in mesh-free methods: (i) constrained mesh-free methods that exploit additional constraint equations to impose continuity of main unknowns and (ii) enrichment of the solution by an appropriate function that reproduces desired properties resulted from the material discontinuity.

DOI: 10.1002/nag

In this work, the second method, as proposed by Belytschko and Krongauz [59], is adopted. This method enriches the basic solution around the line of discontinuity by the proposed functions with the properties of compact support and discontinuous first derivatives. In contrast to the Lagrange multipliers method, only minor oscillations around the line of discontinuity exist [59], and dissimilar to the penalty method, the precision of enforcing material discontinuity does not depend on the user's predefined coefficients.

Nevertheless, a Lagrange multiplier constraining equation is coupled to the system of equations to impose the essential boundaries as additional conditions (see [16, 60–62]). After a concise derivation of governing equations for multiphase iso-thermal porous media, the weak form of the governing equations are developed. Because of the nonlinearities of equations in fluid phases in the case of partially saturated porous systems, additional experimentally defined equations are exploited and a linearization of equations using the Newton–Raphson strategy is performed. Adopting an enriched MLS approximation for field variables, the discretized form of enriched system matrices are derived. Simulations of well-known poro-elasticity problems allow for assessment of enrichment strategies for capturing existing strong and weak discontinuities. The results are discussed for impermeable discontinuities, which lead to discontinuous pressure fields with no fluid exchange through discontinuity walls and material interfaces in the framework of fully coupled deformable saturated and partially saturated porous media.

2. GOVERNING EQUATIONS FOR FULLY COUPLED PARTIALLY SATURATED MULTIPHASE POROUS MEDIA

The governing equations are developed for the general case of partially saturated three-phase deformable porous media undergoing small elastic deformations. Solid phase displacements (**u**), water pressure (p_w), and gas pressure (p_a) are considered as the main variables.

Assuming multiple fluid phases as distinct wetting and nonwetting immiscible parts, existence of any phase change during the fluid flow process is ignored. No heat exchange is present, and only equations of momentum and mass balance for each phase are applied. The whole system is assumed to be working under slow phenomena condition (consolidation), and all inertia and convective terms are droped out from the fully coupled system of equations.

The phenomenological approach of Biot is extended for multiphase partially saturated porous media. Neglecting all convective and inertia terms, the linear balance of momentum equation for the total multiphase system is written as

$$\boldsymbol{L}_{\boldsymbol{u}}^{\boldsymbol{T}}.\boldsymbol{\sigma} + \rho \boldsymbol{b} = 0 \tag{1}$$

where $\boldsymbol{b}$ is the body force vector and ρ is defined as

$$\rho = (1-n)\rho_s + n S_w \rho_w + (1-n) S_a \rho_a \tag{2}$$

where n is the porosity of soil mass and ρ_w and ρ_a are the fluid densities. The modified effective stress is defined as

$$\boldsymbol{\sigma''} = \boldsymbol{\sigma} + \alpha \boldsymbol{m}(S_w p_w + S_a p_a) \tag{3}$$

where $\boldsymbol{\sigma}$ and $\boldsymbol{\sigma''}$ are the total and effective stress vectors, respectively, S_w and S_a are the degrees of saturation for water and gas phases, respectively, and $\mathbf{m} = \begin{bmatrix} 1 & 0 & 0 \end{bmatrix}^T$. α is the Biot's constant and is defined by

$$\alpha = 1 - \frac{K_T}{K_s} \tag{4}$$

in which K_T and K_s are the bulk modulus of porous skeleton and solid grains, respectively. The constitutive relation for the solid phase is written in an incremental form that is more suitable for nonlinear problems:

$$d\boldsymbol{\sigma''} = \mathbf{D}^{\mathbf{T}}(d\boldsymbol{\epsilon}) \tag{5}$$

DOI: 10.1002/nag

where $\mathbf{D^T}$ is the material tangent stiffness matrix, which is simplified to the elastic stiffness tensor $\mathbf{D}$ for linear elastic materials considered in this work (see equation (A.1)).

Writing the momentum balance equation for each phase leads to the well-known generalized Darcy equation for phase α:

$$\boldsymbol{v}^{\alpha s} = \frac{\boldsymbol{k} k_{r\alpha}}{\mu_\alpha}[-\nabla p_\alpha + \rho_\alpha \boldsymbol{b}] \qquad \alpha = w, a \tag{6}$$

where $\boldsymbol{v}^{\alpha s}$ is defined as the relative velocity for phase α with respect to the solid phase. $k_{r\alpha}$ is the relative permeability of phase α and stands for modification in permeability value of phase α due to interaction with multiple fluid flows. $\boldsymbol{k}$ is the intrinsic permeability of medium and is equivalent to the permeability of a fully saturated state. In practice, an experimental relation for $k_{r\alpha}$ in terms of the water saturation and capillary pressures is assumed.

Assuming no mass exchange between the phases, the mass balance equation for phase α is written as

$$\frac{\partial \rho_\alpha}{\partial t} + \rho_\alpha \nabla . \boldsymbol{v_\alpha} = 0 \tag{7}$$

Adding mass balances of each fluid phase multiplied by its corresponding volume fraction to the mass balance equation of solid phase gives the following continuity equation for phase α:

$$\frac{(1-n)}{\rho_s}\frac{\partial \rho_s}{\partial t} + \nabla . \boldsymbol{v_s} + \frac{n}{\rho_\alpha}\frac{\partial \rho_\alpha}{\partial t} + \frac{n}{S_\alpha}\frac{\partial S_\alpha}{\partial t} + \frac{1}{S_\alpha \rho_\alpha}(n S_\alpha \rho_\alpha \boldsymbol{v^{\alpha s}}) = 0 \tag{8}$$

The time derivative of solid density and solid phase pressure are related by the following equation [5]:

$$\frac{1}{\rho_s}\frac{\partial \rho_s}{\partial t} = \frac{1}{1-n}\left[(\alpha - n)\frac{1}{K_s}\frac{\partial p_s}{\partial t} - (1-\alpha)\nabla . \boldsymbol{v_s}\right] \tag{9}$$

Assuming water saturation to be a function of capillary pressure, its time derivative can be written as

$$\frac{\partial S_w}{\partial t} = \frac{\partial S_w}{\partial p_c}\frac{\partial p_c}{\partial t} = \frac{\partial S_w}{\partial p_c}\frac{\partial p_a}{\partial t} - \frac{\partial S_w}{\partial p_c}\frac{\partial p_w}{\partial t} \tag{10}$$

in which $p_c = p_a - p_w$ and the value of $\frac{\partial S_w}{\partial p_c}$ is determined from experimental relations. On the basis of the equation of state for fluid phases, one can write

$$\frac{1}{\rho_\alpha}\frac{\partial \rho_\alpha}{\partial t} = \frac{1}{K_\alpha}\frac{\partial p_\alpha}{\partial t} \tag{11}$$

Incorporating the appropriate constitutive relations (9), (10), and (11) into equation (8), and the Darcy relations for water and gas phases (6) multiplied by their corresponding values of saturation, the following continuity equations for water and gas phases are obtained after lengthy manipulations.

The continuity equation for the water phase flow [5]

$$\begin{aligned}
&\left[S_w \frac{(\alpha - n)}{K_s}\left(S_w + \frac{\partial S_w}{\partial p_c}p_c\right) + \frac{n.S_w}{K_w} - n\frac{\partial S_w}{\partial p_c}\right]\frac{\partial p_w}{\partial t} + \\
&\left[S_w \frac{\alpha - n}{K_s}\left(1 - S_w - \frac{\partial S_w}{\partial p_c}p_c\right) + n\frac{\partial S_w}{\partial p_c}\right]\frac{\partial p_a}{\partial t} + \\
&\alpha S_w \nabla . \boldsymbol{v_s} + \nabla . [\boldsymbol{k_w}(-\nabla p_w + \rho_w(\boldsymbol{b}))] = 0
\end{aligned} \tag{12}$$

The continuity equation for the gas phase flow [5]

$$\begin{aligned}
&\left[(1-S_w)\frac{(\alpha - n)}{K_s}\left(S_w + \frac{\partial S_w}{\partial p_c}p_c\right) + n\frac{\partial S_w}{\partial p_c}\right]\frac{\partial p_w}{\partial t} + \\
&\left[(1-S_w)\frac{\alpha - n}{K_s}\left(1 - S_w - \frac{\partial S_w}{\partial p_c}p_c\right) - n\frac{\partial S_w}{\partial p_c} + \frac{n(1-S_w)}{K_a}\right]\frac{\partial p_a}{\partial t} + \\
&\alpha(1-S_w)\nabla . \boldsymbol{v_s} + \nabla . [\boldsymbol{k_a}(-\nabla p_w + \rho_w(\boldsymbol{b}))] = 0
\end{aligned} \tag{13}$$

DOI: 10.1002/nag

and a set of essential and natural boundary conditions on external and internal boundaries

$$\begin{aligned} \boldsymbol{u} &= \bar{\boldsymbol{u}} \quad on \quad \Gamma_u \\ p_w &= \bar{p_w} \quad on \quad \Gamma_{p_w} \\ p_a &= \bar{p_a} \quad on \quad \Gamma_{p_a} \end{aligned} \tag{14}$$

$$\begin{aligned} \boldsymbol{\sigma}.\boldsymbol{n}_{\boldsymbol{\Gamma_t}} &= \bar{\boldsymbol{t}} \quad on \quad \Gamma_t \\ \boldsymbol{v_w}.\boldsymbol{n}_{\boldsymbol{\Gamma_w}} &= \bar{q_w} \quad on \quad \Gamma_{q_w} \\ \boldsymbol{v_a}.\boldsymbol{n}_{\boldsymbol{\Gamma_a}} &= \bar{q_a} \quad on \quad \Gamma_{q_a} \end{aligned} \tag{15}$$

$$\begin{aligned} \boldsymbol{\sigma}.\boldsymbol{n}_{\boldsymbol{\Gamma_c}} &= 0 \quad on \quad \Gamma_c \\ [\![\boldsymbol{v_w}]\!].\boldsymbol{n}_{\boldsymbol{\Gamma_c}} &= 0 \quad on \quad \Gamma_c \\ [\![\boldsymbol{v_a}]\!].\boldsymbol{n}_{\boldsymbol{\Gamma_c}} &= 0 \quad on \quad \Gamma_c \end{aligned} \tag{16}$$

where $\bar{\mathbf{u}}$, $\bar{p_w}$, and $\bar{p_a}$ are defined as the prescribed values on the essential boundaries Γ_u, Γ_{p_w}, and Γ_{p_a}, respectively. Simultaneously, $\bar{\mathbf{t}}, \bar{q_w}$, and $\bar{q_a}$ are the rate of external force and flux vectors on natural boundaries of Γ_t, Γ_{q_w}, and Γ_{q_a}. $\mathbf{n}_{\mathbf{\Gamma_t}}, \mathbf{n}_{\mathbf{\Gamma_w}}$, and $\mathbf{n}_{\mathbf{\Gamma_a}}$ are the unit normal vectors to external boundaries and $\mathbf{n}_{\mathbf{\Gamma_c}}$ represents the unit normal vector to the discontinuity line. $[\![\boldsymbol{v_w}]\!]$ and $[\![\boldsymbol{v_a}]\!]$ represent the amount of water and gas fluxes attracted to the discontinuity. Equation (16) is the additional condition that holds along the strong discontinuity surface (Γ_c) and confirms the assumption of traction-free discontinuity with no fluid exchange along the discontinuity surfaces. Therefore, the whole state of a partially saturated multiphase deforming porous medium under static loading is expressed by the momentum balance equation of multiphase system (1), the continuity equation of water phase (12), and the continuity equation of gas phase (13) along with appropriate boundary conditions of (14), (15), and (16). The solid displacements, water pressure, and gas pressure are assumed to be the primary unknowns, and the water saturation degree (S_w) and the relative permeability of phases ($k_{r\alpha}$) are introduced to the system of equations based on the experimentally defined relations for capillary pressures.

3. NUMERICAL IMPLEMENTATION

The Bubnov–Galerkin method, in which both the test and trial functions are replaced by the MLS shape functions, is adopted to discretize the constrained weak form of developed governing equations by the EFG method.

The MLS shape approximations lack the property of Kronecker delta function suitable for handling essential boundaries. As a result, imposition of boundary conditions can not be simply performed by replacing the values of prescribed boundaries for the unknowns, as it is the case for finite element solutions. Instead, a constrained set of governing equations must be satisfied. Here, the Lagrange multipliers method is adopted.

Using a weighted residual method, the following constrained Galerkin weak form of the linear momentum balance equation (1) is derived:

$$\int_\Omega \delta(\boldsymbol{L_u u})^T(\boldsymbol{\sigma})d\Omega - \int_\Omega \delta\boldsymbol{u^T b}\,d\Omega - \int_{\Gamma_t} \delta\boldsymbol{u^T}\bar{\boldsymbol{t}}\,d\Gamma_t - \delta\left(\int_{\Gamma_u} \boldsymbol{\lambda_u^T}(\boldsymbol{u}-\bar{\boldsymbol{u}})d\Gamma_u\right) = 0 \tag{17}$$

The same methodology can be applied to the continuity equations of water phase (12) and gas phase (13),

$$\begin{aligned} &\int_\Omega \delta(p_w)^T\left[S_w\frac{(\alpha-n)}{K_s}\left(S_w+\frac{\partial S_w}{\partial p_c}p_c\right)+\frac{nS_w}{K_w}-n\frac{\partial S_w}{\partial p_c}\right]\frac{\partial p_w}{\partial t}d\Omega + \\ &\int_\Omega \delta(p_w)^T\left[S_w\frac{\alpha-n}{K_s}\left(1-S_w-\frac{\partial S_w}{\partial p_c}p_c\right)+n\frac{\partial S_w}{\partial p_c}\right]\frac{\partial p_a}{\partial t}d\Omega + \\ &\int_\Omega \delta(p_w)^T\alpha\boldsymbol{m^T}S_w\boldsymbol{L_u}\frac{\partial \boldsymbol{u}}{\partial t}d\Omega + \int_\Omega \delta\left(\boldsymbol{L_{p_w}}p_w\right)^T[\boldsymbol{k_w}(-\nabla p_w+\rho_w(\boldsymbol{b}))]d\Omega + \\ &\int_{\Gamma_{q_w}} \delta(p_w)^T\bar{q}_w\,d\Gamma_{q_w} - \delta\left(\int_{\Gamma_{p_w}} \lambda_{p_w}^T\left(p_w-\bar{p_w}\right)d\Gamma_{p_w}\right) = 0 \end{aligned} \tag{18}$$

DOI: 10.1002/nag

$$
\begin{aligned}
&\int_{\Omega} \delta(p_a)^T \left[(1-S_w) \frac{(\alpha-n)}{K_s} \left(S_w + \frac{\partial S_w}{\partial p_c} p_c \right) + n \frac{\partial S_w}{\partial p_c} \right] \frac{\partial p_w}{\partial t} d\Omega + \\
&\int_{\Omega} \delta(p_a)^T \left[(1-S_w) \frac{\alpha-n}{K_s} \left(1 - S_w - \frac{\partial S_w}{\partial p_c} p_c \right) - n \frac{\partial S_w}{\partial p_c} + \frac{n(1-S_w)}{K_a} \right] \frac{\partial p_a}{\partial t} d\Omega + \\
&\int_{\Omega} \delta(p_a)^T \alpha (1-S_w) \mathbf{m}^{\mathbf{T}} \mathbf{L_u} \frac{\partial \mathbf{u}}{\partial t} d\Omega + \int_{\Omega} \delta \left(\mathbf{L_{p_a}} p_a \right)^T \left[\mathbf{k_a} (-\nabla p_a + \rho_a(\mathbf{b})) \right] d\Omega + \\
&\int_{\Gamma_{qa}} \delta(p_a)^T \bar{q_a} d\Gamma_{qa} - \delta \left(\int_{\Gamma_{pa}} \lambda_{pa}^T \left(p_a - \bar{p_a} \right) d\Gamma_{pa} \right) = 0
\end{aligned}
\tag{19}
$$

where $\delta(u), \delta(p_w)$, and $\delta(p_a)$ are variations of solid displacement, water pressure, and gas pressure, respectively. $\mathbf{L_u}, \mathbf{L_{p_w}}$, and $\mathbf{L_{p_a}}$ are the differential operators defined as

$$
\mathbf{L_u} = \begin{bmatrix} \frac{\partial}{\partial x} & 0 \\ 0 & \frac{\partial}{\partial y} \\ \frac{\partial}{\partial y} & \frac{\partial}{\partial x} \end{bmatrix}, \qquad \mathbf{L_{p_w}} = \mathbf{L_{p_a}} = \begin{bmatrix} \frac{\partial}{\partial x} \\ \frac{\partial}{\partial y} \end{bmatrix} \tag{20}
$$

As explained before, solid displacement (u), water pressure (p_w), and gas pressure (p_a) are taken as the main unknowns. On the basis of the enrichment strategy to capture discontinuities, values of the unknowns at an arbitrary point x of the domain are approximated by the enriched MLS approximations,

$$
\begin{aligned}
u^h(x) &= \sum_{I=1}^{n_{std}} \Phi_I^{u,std}(x) \boldsymbol{u_I}^{std} + \sum_{I=1}^{n_{enr}} \Phi_I^{u,enr}(x) \boldsymbol{u_I}^{enr} \\
p_w^h(x) &= \sum_{I=1}^{n_{std}} \Phi_I^{p_w,std}(x) \left(p_w^{std} \right)_I + \sum_{I=1}^{n_{enr}} \Phi_I^{p_w,enr}(x) \left(p_w^{enr} \right)_I \\
p_a^h(x) &= \sum_{I=1}^{n_{std}} \Phi_I^{p_a,std}(x) \left(p_a^{std} \right)_I + \sum_{I=1}^{n_{enr}} \Phi_I^{p_a,enr}(x) \left(p_a^{enr} \right)_I
\end{aligned}
\tag{21}
$$

where $\Phi_I^{u,std}$, $\Phi_I^{p_w,std}$, and $\Phi_I^{p_a,std}$ are the standard MLS shape functions and $\Phi_I^{u,enr}$, $\Phi_I^{p_w,enr}$, and $\Phi_I^{p_a,enr}$ represent different enrichment functions defined in Section 4. n_{std} is the number of nodes in the regular support domain and n_{enr} is defined as the number of extra DOFs in the support domain of point x.

Putting the enriched approximations (21) and the effective stress (3) into equations (17), (18), and (19) and after some algebraic and variational manipulations, the complete discretized set of constrained equations for a fully coupled partially saturated three-phase deforming porous medium is obtained:

$$
\begin{aligned}
&\mathbf{K^{n+1}} \boldsymbol{U}^{n+1} - \mathbf{C_{sw}^{n+1}} \boldsymbol{P_w}^{n+1} - \mathbf{C_{sa}^{n+1}} \boldsymbol{P_a}^{n+1} = \boldsymbol{F_u}^{n+1} - \mathbf{G_{\bar{u}}^T} \boldsymbol{\lambda_u^{n+1}} \\
&\mathbf{C_{ws}^{n+1}} \dot{\boldsymbol{U}}^{\boldsymbol{n+1}} + \mathbf{P_{ww}^{n+1}} \dot{\boldsymbol{P}}_{\boldsymbol{w}}^{\boldsymbol{n+1}} + \mathbf{C_{wa}^{n+1}} \dot{\boldsymbol{P}}_{\boldsymbol{a}}^{\boldsymbol{n+1}} + \mathbf{H_{ww}^{n+1}} \boldsymbol{P_w^{n+1}} = \boldsymbol{F_w}^{n+1} - \mathbf{G_{\bar{p}_w}^T} \boldsymbol{\lambda_{pw}^{n+1}} \\
&\mathbf{C_{as}^{n+1}} \dot{\boldsymbol{U}}^{\boldsymbol{n+1}} + \mathbf{C_{aw}^{n+1}} \dot{\boldsymbol{P}}_{\boldsymbol{w}}^{\boldsymbol{n+1}} + \mathbf{P_{aa}^{n+1}} \dot{\boldsymbol{P}}_{\boldsymbol{a}}^{\boldsymbol{n+1}} + \mathbf{H_{aa}^{n+1}} \boldsymbol{P_a^{n+1}} = \boldsymbol{F_a^{n+1}} - \mathbf{G_{\bar{p}_a}^T} \boldsymbol{\lambda_{pa}^{n+1}}
\end{aligned}
\tag{22}
$$

along with the set of constraint equations

$$
\begin{aligned}
\bar{\boldsymbol{U}} &= \mathbf{G_{\bar{u}}} \boldsymbol{U}^{n+1} \\
\bar{\boldsymbol{P}}_{\boldsymbol{w}} &= \mathbf{G_{\bar{p}_w}} \boldsymbol{P_w}^{n+1} \\
\bar{\boldsymbol{P}}_{\boldsymbol{a}} &= \mathbf{G_{\bar{p}_a}} \boldsymbol{P_a}^{n+1}
\end{aligned}
\tag{23}
$$

DOI: 10.1002/nag

where

$$
\begin{aligned}
(\mathbf{G}_{\bar{\mathbf{u}}})_{IK} &= -\int_{\Gamma_u} \Phi_I^u N_k \, d\Gamma_u \\
\left(\mathbf{G}_{\bar{\mathbf{p}}_\mathbf{w}}\right)_{IK} &= -\int_{\Gamma_{pw}} \Phi_I^{p_w} N_k \, d\Gamma_{p_w} \\
\left(\mathbf{G}_{\bar{\mathbf{p}}_\mathbf{a}}\right)_{IK} &= -\int_{\Gamma_{pa}} \Phi_I^{p_a} N_k \, d\Gamma_{p_a}
\end{aligned}
\tag{24}
$$

$N_k(x) = \delta(x - x_k)$, and x_k represents the set of points located along the essential boundaries. $\bar{\boldsymbol{U}}$, $\bar{\boldsymbol{P}}_{\boldsymbol{w}}$, and $\bar{\boldsymbol{P}}_{\boldsymbol{a}}$ are the vectors of prescribed essential boundaries over x_k. A detailed description of the system matrices/vectors in equation (22) is given in Appendix A.

The time derivatives of unknown variables are obtained by assuming a linear variation of the unknown variables in each time step,

$$
\dot{\boldsymbol{U}}^{\boldsymbol{n+1}} = \frac{\boldsymbol{U}^{\boldsymbol{n+1}} - \boldsymbol{U}^{\boldsymbol{n}}}{\Delta t}, \qquad \dot{\boldsymbol{P}}_{\boldsymbol{w}}^{\boldsymbol{n+1}} = \frac{\boldsymbol{P}_{\boldsymbol{w}}^{\boldsymbol{n+1}} - \boldsymbol{p}_{\boldsymbol{w}}^{\boldsymbol{n}}}{\Delta t}, \qquad \dot{\boldsymbol{P}}_{\boldsymbol{a}}^{\boldsymbol{n+1}} = \frac{\boldsymbol{P}_{\boldsymbol{a}}^{\boldsymbol{n+1}} - \boldsymbol{p}_{\boldsymbol{a}}^{\boldsymbol{n}}}{\Delta t} \tag{25}
$$

Putting (25) in the total constrained system of equations (22) and using the Newton–Raphson method, the following equations for the fully coupled formulation can be written as

$$
\begin{aligned}
\boldsymbol{R}_{\boldsymbol{u}}^{\boldsymbol{i,n+1}} &= \boldsymbol{K}^{\boldsymbol{n+1}} \boldsymbol{U}^{i,n+1} - \boldsymbol{C}_{\boldsymbol{sw}}^{\boldsymbol{n+1}} \boldsymbol{P}_{\boldsymbol{w}}^{\boldsymbol{i,n+1}} - \boldsymbol{C}_{\boldsymbol{sa}}^{\boldsymbol{n+1}} \boldsymbol{P}_{\boldsymbol{a}}^{\boldsymbol{i,n+1}} - \boldsymbol{F}_{\boldsymbol{u}}^{\boldsymbol{n+1}} + \boldsymbol{G}_{\bar{\boldsymbol{u}}}^{\boldsymbol{T}} \boldsymbol{\lambda}_{\boldsymbol{u}}^{\boldsymbol{n+1}} \\
\boldsymbol{R}_{\boldsymbol{pw}}^{\boldsymbol{i,n+1}} &= \boldsymbol{C}_{\boldsymbol{ws}}^{\boldsymbol{n+1}} \left(\frac{\mathbf{U}^{\mathbf{n+1}} - \mathbf{U}^{\mathbf{n}}}{\Delta t} \right) + \boldsymbol{P}_{\boldsymbol{ww}}^{\boldsymbol{n+1}} \left(\frac{\mathbf{P}_{\mathbf{w}}^{\mathbf{n+1}} - \mathbf{P}_{\mathbf{w}}^{\mathbf{n}}}{\Delta t} \right) + \boldsymbol{C}_{\boldsymbol{wa}}^{\boldsymbol{n+1}} \left(\frac{\mathbf{P}_{\mathbf{a}}^{\mathbf{n+1}} - \mathbf{P}_{\mathbf{a}}^{\mathbf{n}}}{\Delta t} \right) \\
&\quad + \boldsymbol{H}_{\boldsymbol{ww}}^{\boldsymbol{n+1}} \mathbf{P}_{\mathbf{w}}^{\mathbf{n+1}} - \boldsymbol{F}_{\boldsymbol{w}}^{\boldsymbol{n+1}} + \mathbf{G}_{\bar{\mathbf{p}}_\mathbf{w}}^{\mathbf{T}} \boldsymbol{\lambda}_{\boldsymbol{pw}}^{\boldsymbol{n+1}} \\
\boldsymbol{R}_{\boldsymbol{pa}}^{\boldsymbol{i,n+1}} &= \boldsymbol{C}_{\boldsymbol{as}}^{\boldsymbol{n+1}} \left(\frac{\mathbf{U}^{\mathbf{n+1}} - \mathbf{U}^{\mathbf{n}}}{\Delta t} \right) + \boldsymbol{C}_{\boldsymbol{aw}}^{\boldsymbol{n+1}} \left(\frac{\mathbf{P}_{\mathbf{w}}^{\mathbf{n+1}} - \mathbf{P}_{\mathbf{w}}^{\mathbf{n}}}{\Delta t} \right) + \boldsymbol{P}_{\boldsymbol{aa}}^{\boldsymbol{n+1}} \left(\frac{\mathbf{P}_{\mathbf{a}}^{\mathbf{n+1}} - \boldsymbol{P}_{\boldsymbol{a}}^{\boldsymbol{n}}}{\Delta t} \right) \\
&\quad + \boldsymbol{H}_{\boldsymbol{aa}}^{\boldsymbol{n+1}} \boldsymbol{P}_{\boldsymbol{a}}^{\boldsymbol{n+1}} - \boldsymbol{F}_{\boldsymbol{a}}^{\boldsymbol{n+1}} + \boldsymbol{G}_{\bar{\boldsymbol{p}}_\boldsymbol{a}}^{\boldsymbol{T}} \boldsymbol{\lambda}_{\boldsymbol{pa}}^{\boldsymbol{n+1}} \\
\boldsymbol{R}_{\boldsymbol{\lambda}_\boldsymbol{u}}^{\boldsymbol{i,n+1}} &= \bar{\boldsymbol{U}} - \boldsymbol{G}_{\bar{\boldsymbol{u}}} \mathbf{U}^{\mathbf{n+1}}, \qquad \boldsymbol{R}_{\boldsymbol{\lambda}_{\boldsymbol{Pw}}}^{\boldsymbol{i,n+1}} = \bar{\boldsymbol{P}}_{\boldsymbol{w}} - \boldsymbol{G}_{\bar{\boldsymbol{p}}_\boldsymbol{w}} \mathbf{P}_{\mathbf{w}}^{\mathbf{n+1}}, \qquad \boldsymbol{R}_{\boldsymbol{\lambda}_{\boldsymbol{pa}}}^{\boldsymbol{i,n+1}} = \bar{\boldsymbol{P}}_{\boldsymbol{a}} - \boldsymbol{G}_{\bar{\boldsymbol{p}}_\boldsymbol{a}} \mathbf{P}_{\mathbf{a}}^{\mathbf{n+1}}
\end{aligned}
\tag{26}
$$

and the unknown and residual vectors can be expressed by

$$
\boldsymbol{X}^{\boldsymbol{i,n+1}} = \begin{Bmatrix} \mathbf{U}^{i,n+1} \\ \mathbf{P}_{\mathbf{w}}{}^{i,n+1} \\ \mathbf{P}_{\mathbf{a}}{}^{i,n+1} \\ \boldsymbol{\lambda}_{\boldsymbol{u}}^{\boldsymbol{i,n+1}} \\ \boldsymbol{\lambda}_{\boldsymbol{pw}}^{\boldsymbol{i,n+1}} \\ \boldsymbol{\lambda}_{\boldsymbol{pa}}^{\boldsymbol{i,n+1}} \end{Bmatrix} \qquad \mathbf{R}^{\mathbf{i,n+1}} = \begin{Bmatrix} \mathbf{R}_{\mathbf{u}}^{\mathbf{i,n+1}} \\ \boldsymbol{R}_{\boldsymbol{pw}}^{\boldsymbol{i,n+1}} \\ \boldsymbol{R}_{\boldsymbol{pa}}^{\boldsymbol{i,n+1}} \\ \boldsymbol{R}_{\boldsymbol{\lambda}_\boldsymbol{u}}^{\boldsymbol{i,n+1}} \\ \boldsymbol{R}_{\boldsymbol{\lambda}_{\boldsymbol{pw}}}^{\boldsymbol{i,n+1}} \\ \boldsymbol{R}_{\boldsymbol{\lambda}_{\boldsymbol{pa}}}^{\boldsymbol{i,n+1}} \end{Bmatrix} \tag{27}
$$

Differentiating the residual with respect to the unknowns vector X gives the Jacobian matrix for the constrained system of equations:

$$
\mathbf{J} = \begin{bmatrix}
\mathbf{K} & -\mathbf{C}_{\mathbf{sw}} & -\mathbf{C}_{\mathbf{sa}} & \mathbf{G}_{\bar{\mathbf{u}}}^{\mathbf{T}} & 0 & 0 \\
\frac{\mathbf{C}_{\mathbf{ws}}}{\Delta t} & \frac{\mathbf{P}_{\mathbf{ww}}}{\Delta t} + \mathbf{H}_{\mathbf{ww}} & \frac{\mathbf{C}_{\mathbf{wa}}}{\Delta t} & 0 & \mathbf{G}_{\bar{\mathbf{p}}_\mathbf{w}}{}^{T} & 0 \\
\frac{\mathbf{C}_{\mathbf{as}}}{\Delta t} & \frac{\mathbf{C}_{\mathbf{aw}}}{\Delta t} & \frac{\mathbf{P}_{\mathbf{aa}}}{\Delta t} + \mathbf{H}_{\mathbf{aa}} & 0 & 0 & \mathbf{G}_{\bar{\mathbf{p}}_\mathbf{a}}^{\mathbf{T}} \\
-\mathbf{G}_{\bar{\mathbf{u}}} & 0 & 0 & 0 & 0 & 0 \\
0 & -\mathbf{G}_{\bar{\mathbf{p}}_\mathbf{w}} & 0 & 0 & 0 & 0 \\
0 & 0 & -\mathbf{G}_{\bar{\mathbf{p}}_\mathbf{a}} & 0 & 0 & 0
\end{bmatrix}
\tag{28}
$$

DOI: 10.1002/nag

The following fully coupled nonlinear system of equations should be solved at each time step to compute the unknown increments.

$$\mathbf{R}^{\mathbf{i+1,n+1}} = \mathbf{R}^{\mathbf{i,n+1}} + \mathbf{J}d\mathbf{X}^{\mathbf{i+1,n+1}} = 0 \tag{29}$$

$$d\mathbf{X}^{\mathbf{i+1,n+1}} = \begin{bmatrix} d\boldsymbol{U}^{i+1,n+1} \\ d\boldsymbol{P}_{\boldsymbol{w}}^{i+1,n+1} \\ d\boldsymbol{P}_{\boldsymbol{a}}^{i+1,n+1} \\ d\boldsymbol{\lambda}_{\boldsymbol{u}}^{i+1,n+1} \\ d\boldsymbol{\lambda}_{\boldsymbol{P_w}}^{i+1,n+1} \\ d\boldsymbol{\lambda}_{\boldsymbol{P_a}}^{i+1,n+1} \end{bmatrix} = \frac{-\mathbf{R}^{\mathbf{i,n+1}}}{\mathbf{J}}. \tag{30}$$

in which $\mathbf{R}^{\mathbf{i,n+1}}$ is given in (27) and is computed as

$$\mathbf{R}^{\mathbf{i,n+1}} = \mathbf{J}\begin{bmatrix} \boldsymbol{U}^{i,n+1} \\ \boldsymbol{P}_{\boldsymbol{w}}^{i,n+1} \\ \boldsymbol{P}_{\boldsymbol{a}}^{i,n+1} \\ \boldsymbol{\lambda}_{\boldsymbol{u}}^{i,n+1} \\ \boldsymbol{\lambda}_{\boldsymbol{p_w}}^{i,n+1} \\ \boldsymbol{\lambda}_{\boldsymbol{p_a}}^{i,n+1} \end{bmatrix} - \begin{bmatrix} \boldsymbol{F_u} \\ \boldsymbol{F_w} \\ \boldsymbol{F_a} \\ \bar{\boldsymbol{U}} \\ \bar{\boldsymbol{P}}_{\boldsymbol{w}} \\ \bar{\boldsymbol{P}}_{\boldsymbol{a}} \end{bmatrix} - \mathbf{P}^{\mathbf{n}} \tag{31}$$

where $\mathbf{P}^{\mathbf{n}}$ is the value of converged solution from the last time step of analysis:

$$\mathbf{P}^{\mathbf{n}} = \begin{bmatrix} 0 \\ \boldsymbol{C_{ws}}\left(\frac{\boldsymbol{U}^{\boldsymbol{n}}}{\Delta t}\right) + \boldsymbol{P_{ww}}\left(\frac{\boldsymbol{P}_{\boldsymbol{w}}^{\boldsymbol{n}}}{\Delta t}\right) + \boldsymbol{C_{wa}}\left(\frac{\boldsymbol{P}_{\boldsymbol{a}}^{\boldsymbol{n}}}{\Delta t}\right) \\ \mathbf{C_{as}}\left(\frac{\mathbf{U}^{\mathbf{n}}}{\Delta t}\right) + \boldsymbol{C_{aw}}\left(\frac{\boldsymbol{P}_{\boldsymbol{w}}^{\boldsymbol{n}}}{\Delta t}\right) + \boldsymbol{P_{aa}}\left(\frac{\boldsymbol{P}_{\boldsymbol{a}}^{\boldsymbol{n}}}{\Delta t}\right) \\ 0 \\ 0 \\ 0 \end{bmatrix} \tag{32}$$

Then, the unknown vector is updated at each iteration until the required convergency is achieved:

$$\begin{bmatrix} \boldsymbol{U}^{i+1,n+1} \\ \boldsymbol{P}_{\boldsymbol{w}}^{i+1,n+1} \\ \boldsymbol{P}_{\boldsymbol{a}}^{i+1,n+1} \\ \boldsymbol{\lambda}_{\boldsymbol{u}}^{i+1,n+1} \\ \boldsymbol{\lambda}_{\boldsymbol{P_w}}^{i+1,n+1} \\ \boldsymbol{\lambda}_{\boldsymbol{p_a}}^{i+1,n+1} \end{bmatrix} = \begin{bmatrix} \boldsymbol{U}^{i,n+1} \\ \boldsymbol{P}_{\boldsymbol{w}}^{i,n+1} \\ \boldsymbol{P}_{\boldsymbol{a}}^{i,n+1} \\ \boldsymbol{\lambda}_{\boldsymbol{u}}^{i,n+1} \\ \boldsymbol{\lambda}_{\boldsymbol{p_w}}^{i,n+1} \\ \boldsymbol{\lambda}_{\boldsymbol{p_a}}^{i,n+1} \end{bmatrix} + \begin{bmatrix} d\boldsymbol{U}^{i+1,n+1} \\ d\boldsymbol{P}_{\boldsymbol{w}}^{i+1,n+1} \\ d\boldsymbol{P}_{\boldsymbol{a}}^{i+1,n+1} \\ d\boldsymbol{\lambda}_{\boldsymbol{u}}^{i+1,n+1} \\ d\boldsymbol{\lambda}_{\boldsymbol{p_w}}^{i+1,n+1} \\ d\boldsymbol{\lambda}_{\boldsymbol{p_a}}^{i+1,n+1} \end{bmatrix} \tag{33}$$

4. ENRICHMENT STRATEGY FOR SIMULATION OF DISCONTINUITIES IN POROUS MEDIA

On the basis of the partition of unity property of MLS shape functions, the approximation field at an arbitrary point x can be defined by (21). Two types of strong and weak enrichments are used in this study.

DOI: 10.1002/nag

4.1. Weak discontinuity enrichments

Because of the continuity of EFG mesh-free method that results in a smooth strain/pressure gradient distribution throughout the domain, handling the material discontinuity cannot be simply performed by just putting a set of nodes at the line of material interface. In fact, instead of a discontinuity in the gradient field of the form of Heaviside function, low accuracy oscillatory results in both unknown fields and their derivatives may occur. To avoid such oscillations, special methods should be incorporated to suitably introduce discontinuity in the first derivatives. In the method presented by Krongauz and Belytschko [59], the field solution at each point intersected by the discontinuity line is defined as a combination of standard EFG solution and a set of additional enrichments parts.

The enrichment functions $\left(\Phi_I^{\alpha,enr} = \psi_J(\bar{r})\right)$ are defined so that to have a compact support domain, ensuring a banded system of equations. These set of enrichment functions retain the continuity in the main variables while their first derivatives are equal to a multiplication of the Heaviside function.

Two sets of enrichment functions $\psi(r)$ are examined:

1 - The first function is a cubic spline function, defined as

$$\psi_{J(\bar{r}_J)} = \begin{Bmatrix} -\frac{1}{6}\bar{r}_J^3 + \frac{1}{2}\bar{r}_J^2 - \frac{1}{2}\bar{r}_J + \frac{1}{6} & \bar{r}_J <= 1 \\ 0 & \bar{r}_J > 1 \end{Bmatrix} \quad ,\bar{r}_J = \frac{r_J}{r_{jc}} \tag{34}$$

in which r_J is the distance from the J'th line of discontinuity and r_{jc} is a characteristic length of the same order as nodal spacing.

2 - The second function is a localized ramp function and is defined by the following expression:

$$\psi_{J(\bar{r}_J)} =< x - x_J > - \sum_I \Phi_I(x) < x_I - x_J > \tag{35}$$

where x_J is the location of weak discontinuity and the ramp function $< x >$ is defined as

$$< x >= \begin{cases} x & \text{if } x \geq 0 \\ 0 & \text{otherwise} \end{cases} \tag{36}$$

Additional DOFs for capturing the weak discontinuity (q^J) are interpolated by one-dimensional shape functions N_I along the line of discontinuity,

$$q_{(s)}^J = N_1 q_1^J + N_2 q_2^J \tag{37}$$

where s is the local coordinate of the projected point along the J'th line of discontinuity.

To assemble the discretized matrices of the system, derivatives of the enrichment functions with reference to the global coordinates x-y are required:

$$\begin{aligned} \frac{du^h}{dx} &= \frac{d}{dx}\left[\sum_{J=1}^{n_d} q^J(s)\psi_J(\bar{r})\right] = \sum_{J=1}^{n_d} \frac{dq^J(s)}{dx}\psi_J(\bar{r}) + \sum_{J=1}^{n_d} \frac{d\psi_J(\bar{r})}{dx} q^J(s) \\ \frac{dq^J(s)}{dx} &= \sum_{I=1}^{2}\left(\frac{dN_I}{ds}\frac{ds}{dx}\right) q_I^J = \left(\frac{dN_1}{ds}\frac{ds}{dx}\right) q_1^J + \left(\frac{dN_2}{ds}\frac{ds}{dx}\right) q_2^J \\ \frac{d\psi_{J(\bar{r})}}{dx} &= \frac{d\psi_{J(\bar{r})}}{dr}\frac{dr}{dx} \end{aligned} \tag{38}$$

It should be mentioned that in contrast to the local enrichment approaches used for strong discontinuities in the extended finite element method or extrinsically enriched mesh-free methods, n_{enr} in equation (21) for the case of weak discontinuity is the number of discontinuity segments rather than being the number of enriched nodes in the support domain of x [59]. Also the effect of enrichment is considered only on gauss points for which the value of enrichment function is nonzero (Figure 1). See [63] for further details on numerical integration and enrichment definition.

DOI: 10.1002/nag

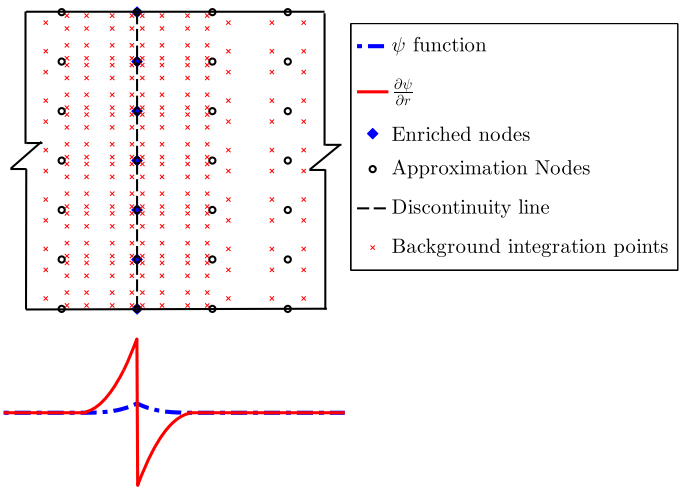

Figure 1. Enriched nodes for weak discontinuity representation.

The following algorithm is used for integration of system of equations:

1 - Loop over integration gauss points
2 - Loop over lines of discontinuity (n_d)
3 - Evaluate the minimum distance from point x to the line segment J of discontinuity ($\bar{r_J}$)
4 - Evaluate the value of enrichment function Ψ_J ($\bar{r}_J$).
5 - Compute system submatrices and assemble the total system of equations.

4.2. Strong discontinuity enrichments

In the case of strong discontinuity, it is assumed that the solid displacement and the water pressure are discontinuous along the discontinuity length. Therefore, the following Heaviside function is used as the enrichment function for both solid and fluid phases along the discontinuity length:

$$H(x) = \begin{cases} 1 & \text{if } (x - x^{cr}).e_n \geq 0 \\ 0 & \text{otherwise} \end{cases} \tag{39}$$

where x^{cr} is the closest point of a discontinuity to the point x and e_n is the normal vector of the discontinuity at point x^{cr}.

For tip enriched nodes, on the basis of the analytical solution of Williams [64], the displacement field is enriched by the following well-known enrichment functions that introduce discontinuity in the displacement field and singularity in the strain field at the discontinuity tip:

$$F_u(r,\theta) = \left[\sqrt{r}sin(\theta) \quad \sqrt{r}cos(\theta) \quad \sqrt{r}sin\left(\frac{\theta}{2}\right)cos(\theta) \quad \sqrt{r}cos\left(\frac{\theta}{2}\right)cos(\theta) \right] \tag{40}$$

For water pressure near a discontinuity tip, on the basis of the solution of pressure fields at a singular point and assuming no fluid exchange across the discontinuity, the following enrichment function is used as the tip enrichment (Khoei *et al.* [46] and Yosibash [65]),

$$B_p(r,\theta) = \sqrt{r}sin\left(\frac{\theta}{2}\right) \tag{41}$$

Function (39) introduces discontinuity in the pressure field and its gradients across the discontinuity, whereas the function (41) produces a singular gradient field at the tip of strong discontinuity. These functions are used throughout this paper for modeling problems, which include additional impermeable strong discontinuities, where no fluid exchange is permitted across the discontinuity [46, 66, 67].

Selection of enriched discontinuity-length and discontinuity-tip nodes are performed by the level set method, developed in [55]. Due to the existence of high gradients at a discontinuity tip, higher order

DOI: 10.1002/nag

integrations must be considered in the near tip region which can be attained by proper subtriangulation of near tip elements. In addition, if the support domain of a node intersects the line of discontinuity, it is enriched only if sufficient integration points exist in both sides of the discontinuity. To avoid numerical instabilities for marginal cases, the support domain can be gradually increased to include sufficient background gauss points at both sides of the intersection.

5. NUMERICAL SIMULATIONS

5.1. One-dimensional consolidation of a soil column

As the first problem a one dimensional multilayer saturated soil column subjected to a constant surface loading is selected. This problem is of the simplest form of problems in multilayer porous media for which the analytical solution is available. A two dimensional plane strain model is constructed with the developed enriched EFG formulation and the results are compared with the reference solutions.

A saturated soil column of 2 m width and 24.384 m height is assumed, and a constant initial surface load of 1 kN is applied at its top edge to reproduce the initial uniform pressure along the column height. The bottom edge is assumed to be fully fixed in all directions, whereas the side edges are constrained only in the horizontal direction. Similar to [68], two different states for water pressure conditions at boundaries are considered. Case I addresses the state in which water is drained from both top and bottom edges, whereas case II represents water drainage from the top boundary only. A total of four layers are considered with material properties defined in Table I. The layers are assumed to have different material properties so as to have a weak discontinuity in solid displacements and water pressures. As an extension to one-dimensional consolidation theory of Terzaghi, which holds for only single layer conditions, the following analytical solution, presented by Schiffman and Stein [69], can be used for a soil layer consisting of n contiguous sublayers and a total thickness of $H = \sum_{i=1}^{n} h_i$

$$
\begin{aligned}
u_i &= \sum_{m=1}^{\infty} g_{mi}(z)\left[C_m e^{-\beta_{mi}t} + D_m \int_0^t \frac{dg}{d\tau} e^{-\beta_{mi}(t-\tau)} d\tau\right].\\
\beta_{mi} &= \lambda_{mi}^2 \frac{c_{vi}}{h_i^2}\\
g_{mi}(z) &= A_{mi} sin\left(\mu_i \lambda_{m1} \frac{z}{h_1}\right) + B_{mi} cos\left(\mu_i \lambda_{m1} \frac{z}{h_1}\right)
\end{aligned}
\tag{42}
$$

in which $i = 1, 2, \ldots, n$. For a more comprehensive explanation on the solution and parameters used in equation (42), see Lee *et al*. [68] and Schiffman and Stein [69].

Geometry of the problem and the uniformly distributed nodes are shown in Figure 2. This figure also shows the selected enriched nodes for describing the material discontinuity and two different enrichment functions of type A and type B and their derivatives defined along the column height. The value of r_{jc} is taken from $(dm/3)$ in which dm is the size of nodal support domain that is constant throughout the domain for the uniform nodal arrangements used in this problem.

Figure 3 shows the results obtained for the water pressure along the column height at times 740, 2930 and 7195 days for the boundary type I compared with the analytical solutions (42), which shows a very good agreement. In addition, Figure 4 illustrates variations of vertical displacements at the interface points for different times.

Table I. Material properties for the problem of multilayer one-dimensional consolidation.

Layer number	Layer height (m)	Young's modulus $\left(\mathrm{KN/m^2}\right)$	Permeability (m/s)
1	3.0480	1.560×10^4	2.8350×10^{-8}
2	6.0960	2.4510×10^4	8.4132×10^{-8}
3	9.1440	4.9020×10^4	1.1931×10^{-8}
4	6.0960	2.4510×10^4	2.9982×10^{-8}

DOI: 10.1002/nag

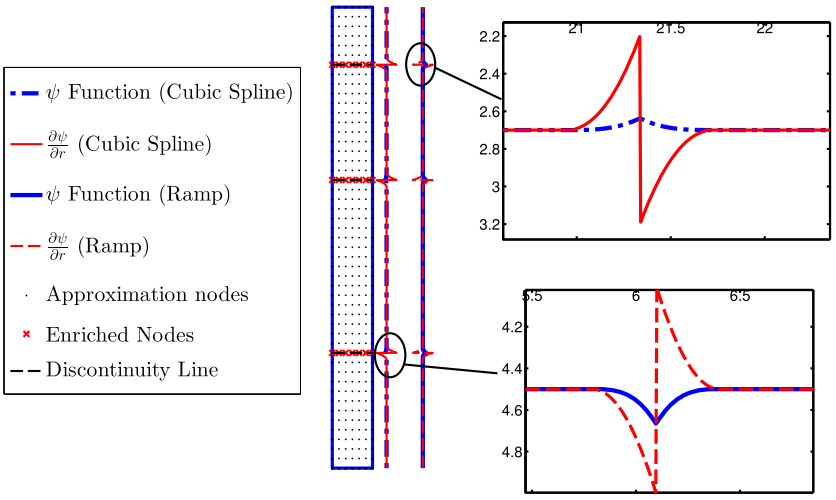

Figure 2. Nodal arrangement for the one-dimensional consolidation example and values of enrichment functions along the column height: up, spline function; down, ramp function.

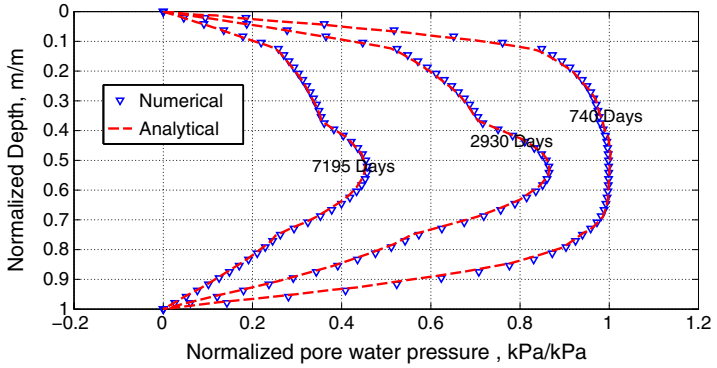

Figure 3. Pore water pressure distribution along the column height (boundary type I).

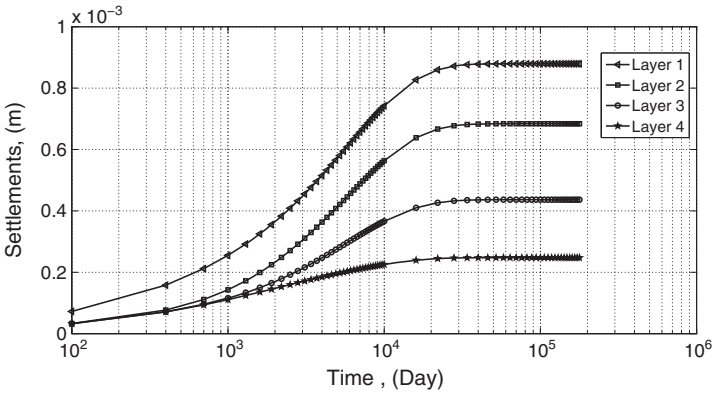

Figure 4. Settlements at layer interfaces (boundary type I).

Figures 5 and 6 show the corresponding values for the boundary type II. Again, the results obtained from the present enriched EFG formulation is in complete agreement with the reference analytical solutions reported by Schiffman and Stein [69] and Lee *et al*. [68].

DOI: 10.1002/nag

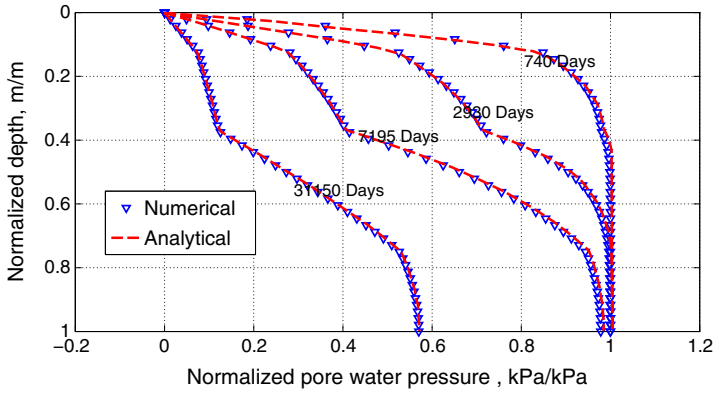

Figure 5. Pore water pressure distribution along the column height (boundary type II).

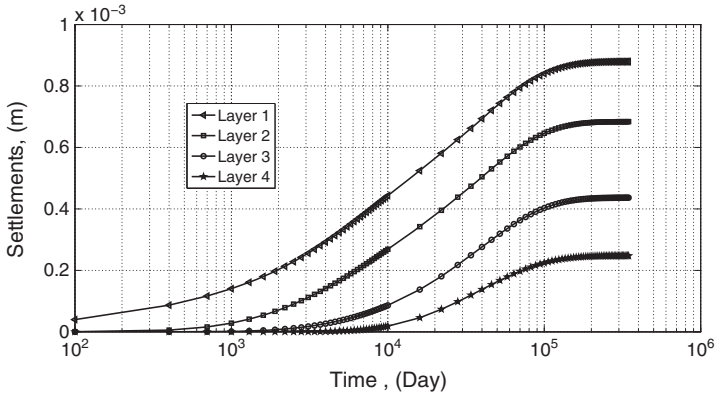

Figure 6. Settlements at layer interfaces (boundary type II).

In order to show the effects of enrichments on predictions of gradient fields, the values of vertical strain (ϵ_{yy}) and gradient of water pressure normal to the discontinuity line are plotted along the column height in figures 7 and 8. It is clear that the unenriched EFG fails to reproduce the existing discontinuity in the first derivatives, whereas the enriched solution captures the discontinuity. The results from the enrichment type B, ramp function (35), show minor oscillations in contrast with the smooth response of the enrichment function type A, representing the cubic spline function (34).

To assess the effects of proposed enriched solution on the convergence of the problem, a convergence test with different uniform nodal arrangements of 51, 132, 342, 873, 2254, and 3417 nodes are examined. L_2 norm of the error in solid displacements and water pressure are computed by the following equations:

$$\|e_{\boldsymbol{u}}\|_{L_2} = \frac{\sqrt{\int_\Omega \|\mathbf{u}(x,t) - \mathbf{u}^{\mathbf{h}}(x,t)\|^2}}{\sqrt{\int_\Omega \|\mathbf{u}(x,t)\|^2}}$$
$$\|e_{p_w}\|_{L_2} = \frac{\sqrt{\int_\Omega \|p_w(x,t) - p_w^h(x,t)\|^2}}{\sqrt{\int_\Omega \|p_w(x,t)\|^2}} \tag{43}$$

where $\mathbf{u}^{\mathbf{h}}(x,t)$ and $p_w^h(x,t)$ are the approximated values for displacement and water pressure, whereas $\mathbf{u}(x,t)$ and $p_w(x,t)$ are the reference displacements and water pressure values. Variations of the convergence ratio resulted from the ramp function, the cubic spline function, and the unenriched EFG for different nodal arrangements for displacements and water pressure are shown in Figure 9. It is clear

DOI: 10.1002/nag

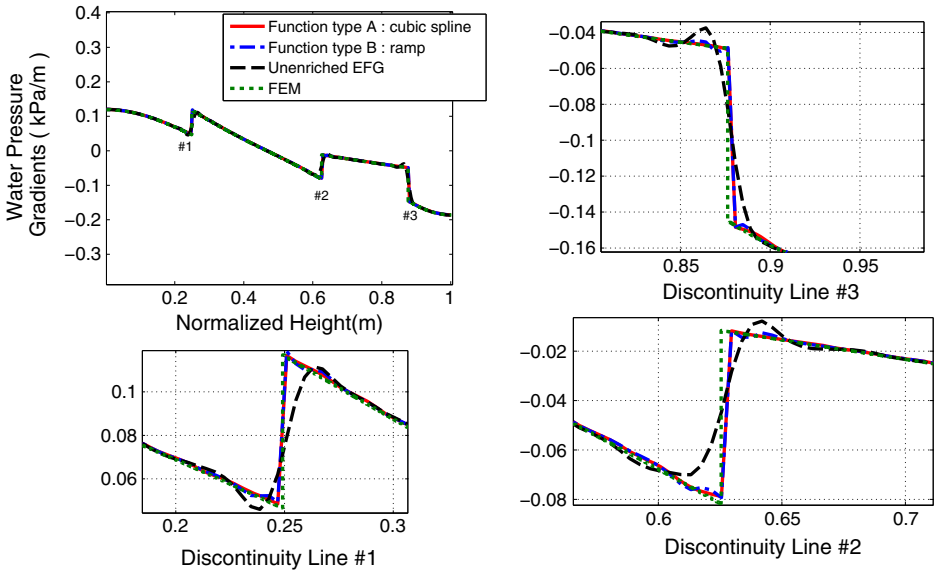

Figure 7. Gradient of water pressure along column height for spline function, ramp function, unenriched EFG method, and FEM at time $t = 3000$ days.

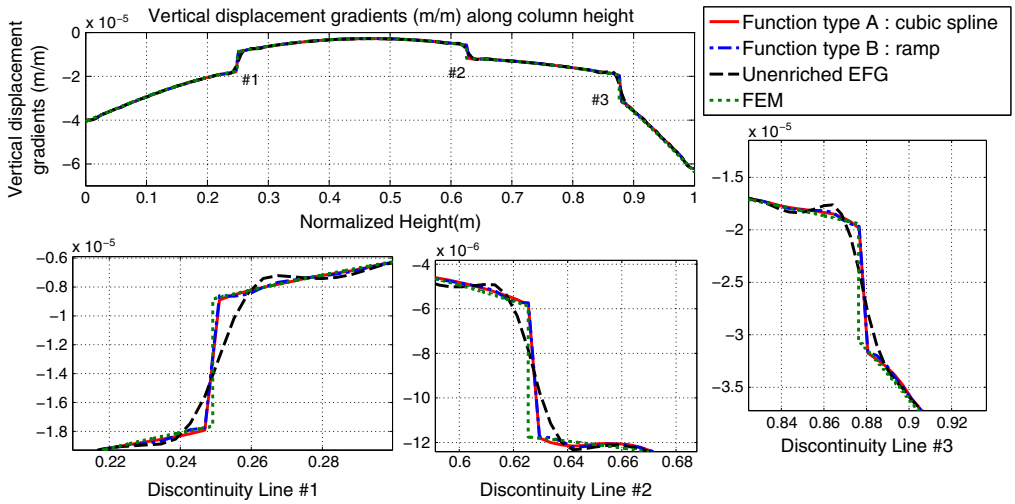

Figure 8. Gradient of vertical displacements along column height for spline function, ramp function, unerniched EFG method, and FEM at time $t = 3000$ days.

that the optimum convergence rate of EFG using a linear basis tends to be a value between 2 and 3 for both water pressure and displacements, which fits the findings of others [17, 19, 70]. Results of unenriched EFG method with no constraints for imposition of weak discontinuity show that neglecting the enrichment part leads to low accurate results with a relatively low rate of convergence for both solid and fluid phases.

5.2. Two-dimensional consolidation of multilayer saturated porous media

Two dimensional problems of consolidation of saturated multilayer soils under strip loadings are considered. First, the problem previously addressed by Booker and small [71], which accounts for two different layers with a material discontinuity at mid-height is solved and then the more complicated

DOI: 10.1002/nag

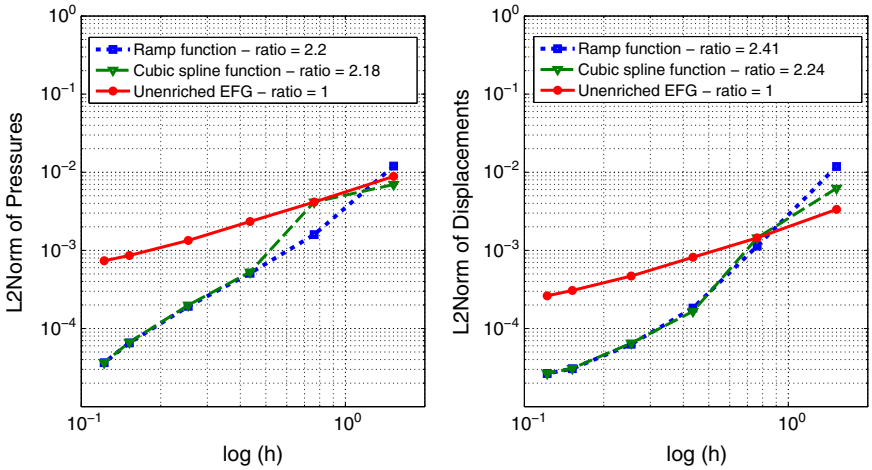

Figure 9. Convergence test results for the problem of multilayered one-dimensional consolidation after 2900 days of analysis.

problem of water seepage through the resting foundation of a dam consisting of different sublayers and in the presence of a cut-off wall is considered.

5.2.1. Double-layer soil foundation under strip loading. Booker and Small [71, 72] introduced semi-analytical solutions based on the Fourier transformation of the governing equations in conjunction with the finite difference method to solve the problem of two-dimensional two-layer soil resting on a rigid base. They also examined the effect of finite boundaries on the solution and determined the minimum width required to eliminate the boundary effects on infinite problems. Therefore, the present model is assumed to be wide enough to ensure that the infinite boundary prevails.

The soil specimen is assumed to have 1 m height and 6 m width, and two equal sublayers with a material discontinuity at the mid-height are assumed.

Two sets of material properties with different values of stiffness and permeability are considered. A discontinuity in the strain field and the pressure gradients is present along material interfaces, meaning that both solid and water phases should be enriched by appropriate functions to properly capture the discontinuity in derivatives. Similar to [71], to study the effects of material discontinuity on solutions, the upper layer is assumed to be less stiff and more permeable. For the upper layer, the Young's modulus is equal to 10^4 Pa, the intrinsic permeability $k = 10^{-7}\mathrm{m}^2$, and the fluid viscosity is taken as 10^{-3} Pa.s. For the lower sublayer, the Young's modulus is set to be double of the upper layer's one, and a lower permeability equal to a quarter of the bottom layer's permeability is adopted. The Poisson's ratio is set to be 0.3 for both layers, and the problem is solved under the plane strain conditions. As a natural boundary condition, a strip load of 1000 kPa is exerted at a length $0 \leq a \leq L$ and held constant during the consolidation analysis. A fully drained boundary for the water pressure is assumed at the top edge while the other boundaries are considered impermeable to fluid flow.

Again, a set of nodes are placed along the line of discontinuity and are enriched by the weak discontinuity functions of (34) and (35) to capture the weak discontinuity in solid displacements and water pressures. The nonuniform nodal arrangements and the enrichment nodes are shown in Figure 10. The problem is solved for two different situations of the resting base: (I) The first type defines a state that displacement constraints are applied in the x direction for the left, bottom and right edges and in the y direction for the bottom edge. (II) the next type enforces displacement constrains along the x and y directions only for the bottom edge. Analytical solutions of a single layer case were presented by Gibson *et al*. [73] by assuming the material properties to be similar to the upper layer of the bi-material case with a zero Poisson's ratio. Figure 11 shows the variations of water pressure and displacements in time for the single layer case and for two different situations of the resting base. It is observed that the reference analytical solutions of Gibson *et al*. [73] and the numerical solutions by Samimi and Pak [23] closely match with the present EFG results.

DOI: 10.1002/nag

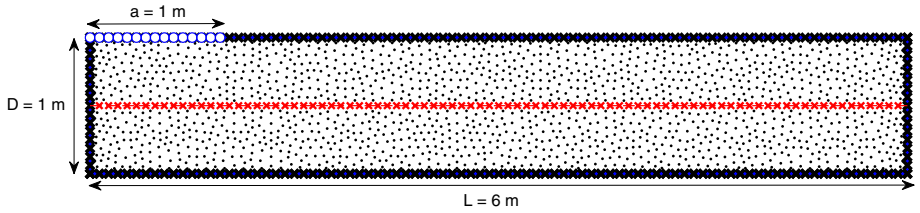

Figure 10. Nodal arrangement for the problem of fully saturated two-layered consolidation.

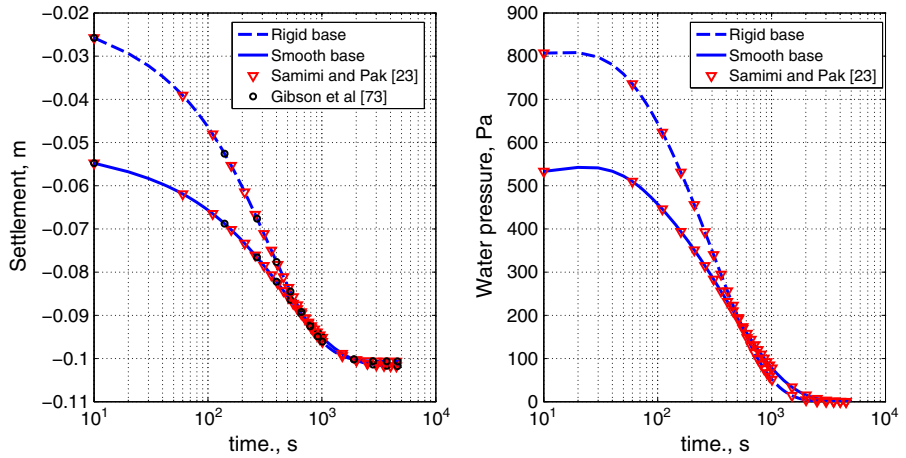

Figure 11. Settlements at the surface of centerline and water pressure distribution at mid-height of centerline for different times of analysis.

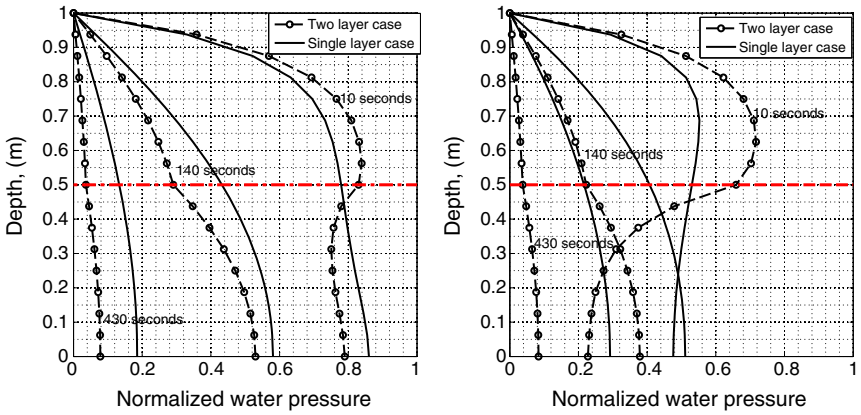

Figure 12. Water pressure distribution along the soil height: left, boundary type I; right, boundary type II.

Water pressure distribution along the column height in the presence of material discontinuity for different cases of resting base is shown in Figure 12. It is observed that even though the lower layer is less permeable, the pore water pressure dissipates faster for the system of two-layer soils for both boundary conditions. The same behavior was reported by Booker and Small which further confirms the good agreement between the numerical and reference results [71]. Distributions of water pressure gradient and vertical strains throughout the two-layer domain are shown in Figure 13, which depicts the values for a set of fine nodes placed along the left edge height to better illustrate the discontinuity in gradients. Again, while the inability of EFG method in reproducing the discontinuous gradients is obvious, the best accuracy belongs to the ramp function (35).

DOI: 10.1002/nag

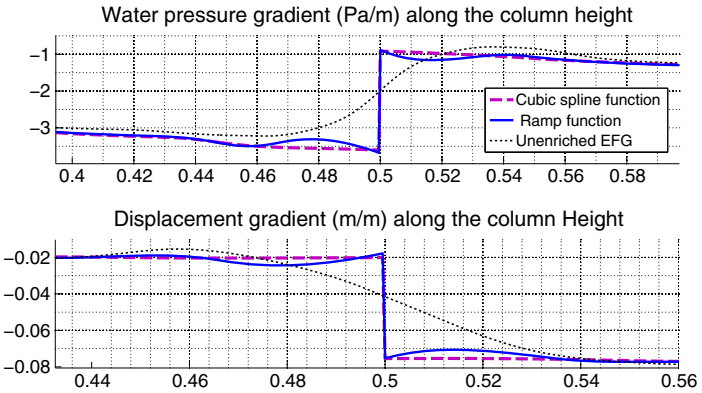

Figure 13. Variations of water pressure gradients and displacement gradient along the soil height for the last time step of the analysis (boundary type I).

It is worth mentioning that because only nodes along the discontinuity line are enriched, the total number of additional DOFs remains relatively low even in comparison with usual extrinsically enriched methods for which a local enrichment strategy is used.

5.2.2. Multimaterial saturated porous medium containing an impermeable discontinuity. The problem of water seepage through the resting foundation of a dam under fully saturated conditions in the presence of a cutoff wall which acts as an impermeable discontinuity is considered. It is assumed that the soil is composed of 4 parallel sublayers and a cutoff wall is placed in a certain distance from the dam's base in order to reduce the amount of water seepage through the soil foundation towards the downstream, as depicted in Figure 14. The height of the domain is 13.5m and its width is 36.5m and the cutoff wall with the length of 5.5m is placed at a distance of 11m from the left edge. The boundary conditions and orientation of discontinuities are plotted at Figure 14.

A series of nodes are placed along the lines of discontinuity to simulate material interfaces as the weak discontinuity lines. To represent the cutoff wall, any node whose support domain intersects the cutoff wall is enriched by the strong discontinuity enrichment functions. The water pressure is assumed to be discontinuous across the cutoff wall, and a singularity in water pressure gradients at the cutoff tip is presumed on the basis of the solutions of water pressure near the singular point.

The dam's weight is considered as a vertical surface load and all other displacement boundaries are constrained along their normal axis direction. For water pressure boundaries, it is assumed that

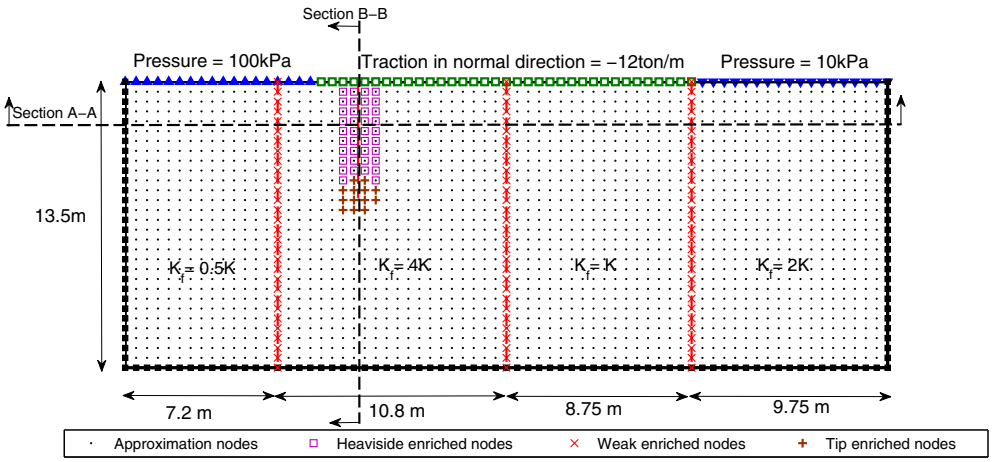

Figure 14. Nodal arrangements for the problem of saturated porous medium with impermeable discontinuity.

DOI: 10.1002/nag

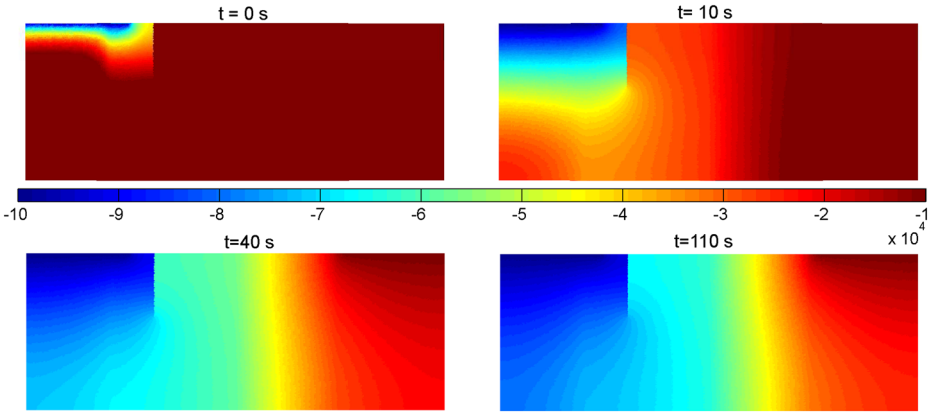

Figure 15. Values of water pressure interpolated at background integration points (Pa).

a constant over-head of 100 kPa exists along the upstream edge, while for the downstream surface a 10 kPa water pressure is applied. Other boundaries are assumed to be impermeable with zero water out-flow. The problem is solved under the plane strain conditions with the Poisson's ratio of 0.4 and the uniform elasticity modulus of $9 \times 10^6 kPa$. Solid and water phase densities are $2 \times 10^6 kg/m^3$ and $1 \times 10^6 kg/m^3$, respectively. The bulk modulus of solid and water are $1 \times 10^{14} MPa$ and $2 \times 10^3 MPa$, respectively, and the porosity is taken as 0.3.

Figure 14 shows the geometry of the problem and the set of nodal arrangements and enriched nodes. It is assumed that all parts of the domain have a uniform mechanical strength but with different permeabilities. The fraction of intrinsic permeability to water density ($K = \mathbf{k}/\mu_w$) is equal to $1 \times 10^{-9} m^2/Pa.s$ while the value of the corresponding fraction for each layer (K_f) is defined in Figure 14. Contours of water pressure at different times are shown at Figure 15. The water pressure becomes discontinuous across the cutoff wall while a singularity in water pressure gradient is expected at the cutoff wall tip due to the use of tip enrichments. Obviously, the proposed enrichments strategy allows proper capture of both strong and weak discontinuities that are present in this problem.

To better illustrate the existing discontinuities in gradient fields along the weak and strong discontinuity lines, a section at the height of 11 m from the base of soil foundation (Section A-A) and a section along the cutoff wall (Section B-B) are considered, as shown in Figure 14. Variations of water pressure gradients normal to the material interfaces for the ramp function, cubic spline function, and unenriched EFG are plotted in Figure 16. Expectedly, the ramp function shows the best performance, whereas the unenriched EFG is unable to capture weak discontinuities. Also, as shown in Figure 17 for Section B-B, an extremely large value for the water pressure gradient is observed at the tip of the cutoff wall, which confirms the proper implementation of tip enrichments, whereas no singularity in the gradient field is present for the case of no tip enrichments.

5.3. Two-phase partially saturated porous media

This section addresses a set of problems of single phase fluid flow in partially saturated media. Using additional experimentally determined relations for the water saturation (S_w) and the relative permeability of water phase (k_{rw}), a fully coupled nonlinear system of equations should then be solved. To assess the performance of developed enriched EFG formulation, two sets of problems in partially saturated media are considered. The first problem examines a soil strata consisting of two distinct sublayers under quasi-static conditions. Then, the same problem is solved in the presence of multiple strong discontinuities.

5.3.1. Consolidation of a two-layer partially saturated porous medium—the Liakopoulos test. This problem is based on the experiments conducted by Liakopoulos [74] on a single layer sand column and has been frequently analyzed by various researchers assuming two-phase and three-phase fluid

DOI: 10.1002/nag

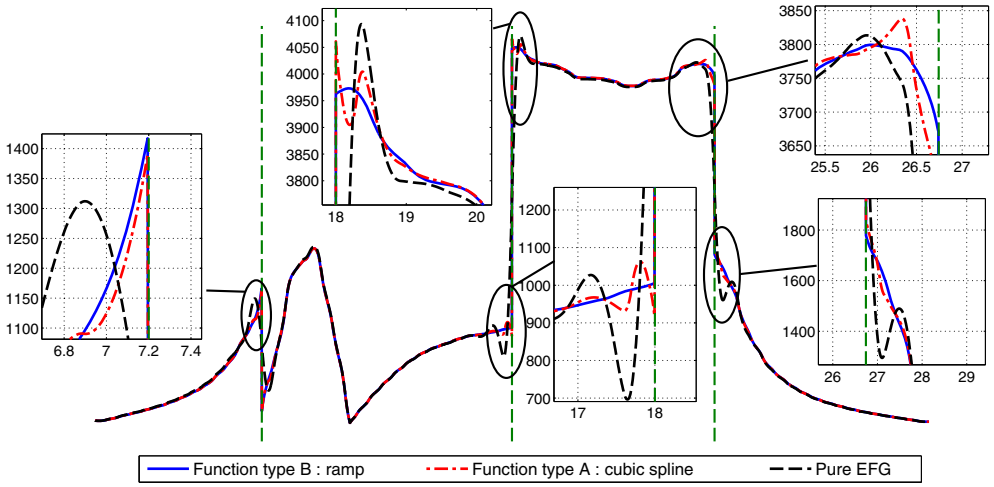

Figure 16. Values of water pressure gradients (Pa/m) along the section A-A of soil layers for the problem of saturated porous medium with discontinuity at time $t = 110$ s.

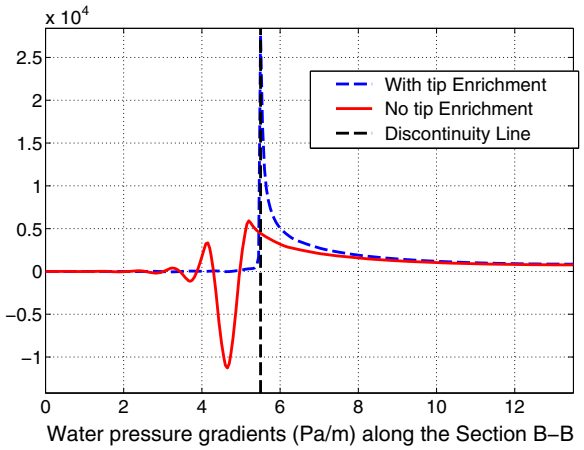

Figure 17. Values of water pressure gradients (Pa/m) along the section B-B of soil layers for the problem of saturated porous medium with discontinuity at time $t = 110$ s.

flow under quasi-static conditions. The material properties used in this experiment are similar to the values used for the upper layer state in Table II.

The test is performed on a 1m high column of packed Del Monte sand, initially subjected to a constant flow of water from its top which results in a uniform water pressure distribution along the column height. Then, the water flow is ceased from the top boundary and all boundaries except for the bottom edge become impermeable to out-ward water flows. No physical load is deemed to be present and as the experiment starts, the water is freely drained from the bottom edge. Deformations along the normal direction to the boundary surfaces are constrained and the value of water pressure is measured along the column height. The width of the specimen is assumed to be 0.1m.

The following experimental relations often used by various researchers are applied for the water saturation and intrinsic permeability of water phase update during the water flow process [7, 11, 75]:

$$\begin{aligned} S_w &= 1 - 0.10152 \left(\frac{p_c}{\rho_w g} \right)^{2.4279} \\ k_{rw} &= 1 - 2.207(1 - S_w)^{1.0121} \end{aligned} \tag{44}$$

DOI: 10.1002/nag

Table II. Material properties for the problem of multilayer partially saturated porous medium.

Material property	Upper layer	Bottom layer
Young modulus (MPa)	1.3	0.13
Solid density (kg/m^3)	2000	2000
Water density (kg/m^3)	1000	1000
Solid bulk modulus (Pa)	1.0×10^{12}	1.0×10^{12}
Fluid bulk modulus (Pa)	2.0×10^{9}	2.0×10^{9}
Water viscosity (Pa.s)	1.0×10^{-3}	1.0×10^{-3}
Intrinsic permeability of water (m^2)	4.5×10^{-13}	1.84×10^{-12}
Layer height (m)	0.5	0.5
Poisson ratio	0.4	0.4
Biot coefficient	1	1
Porosity	0.2975	0.2975

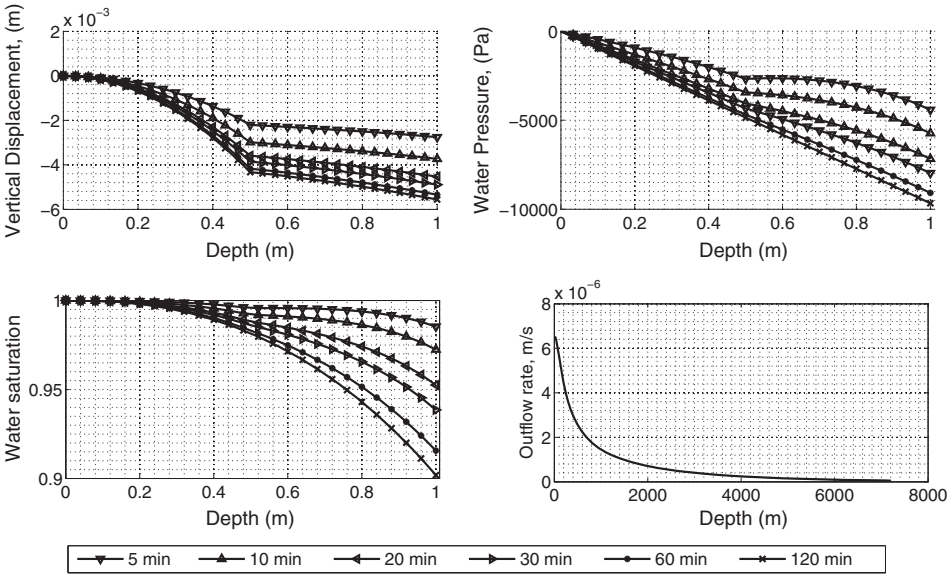

Figure 18. Results of water drainage for the two-layer soil column.

in which $p_c = -p_w$, S_w is the amount of water saturation and ρ_w is the water density. The soil column is initially fully saturated with zero gradients of water pressure along the column height (constant pressure in height), but as the water starts to drain from the lower edge, the soil column is desaturated on the basis of the experimentally defined relations of (44), which is a function of water pressure. Analysis continues for a total duration of 2 h in which the final static equilibrium state is recovered. The initial time step is taken as 10 s, and after the first hour of consolidation, as the flow process rate decreases, an increased value of time step is preferred.

Here, the presence of material discontinuity is studied. The soil column is assumed to be composed of two different layers with an interface at mid-height. Table II summarizes different material properties used in this problem. The problem is solved with the assumption of presence of passive gas pressure and material discontinuity in both water flow and displacements gradient normal to the line of discontinuity. Both the displacements and the water pressure fields are enriched and the results for the cubic spline and the localized ramp functions are evaluated.

A total of 155 nodes (5×31) are used, and the size of nodal support domain (di) is set to 0.0467.

Variations of water pressure, water saturations and displacements along the column height are shown in Figure 18. The sudden changes in slope of water pressure and displacement fields are due to the material interface and the existence of discontinuity in the gradient fields. As expected, it is also

DOI: 10.1002/nag

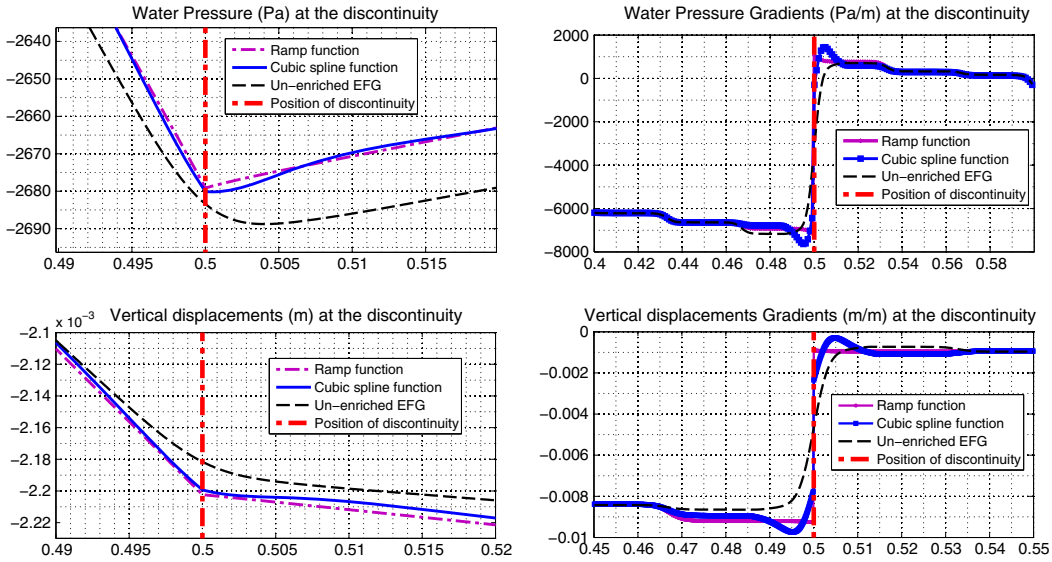

Figure 19. Results at a fine scale around the discontinuity line.

apparent from the figures that for the multilayer system because of greater values of permeabilities, the final state of water pressures for an equal instant of time is greater than the single layer case [5] and the final equilibrium state is reached in less number of time steps. In addition, it is observed that larger amount of outward flow exists for the multilayer model; i.e. more water is drained from the lower edge.

In order to further examine the effect of enrichments, Figure 19 shows the distributions of water pressure and displacements and their gradients at the region of material discontinuity for both enriched and unenriched EFG at 10 minutes after the start of the analysis. Results are produced from a set of dense nodes placed along the column height in order to capture the material discontinuity properties with a good resolution. Clearly, both the ramp function and the cubic spline function reproduce a sudden change in slopes of water pressure and displacements while values of water pressure and solid displacements remain continuous along the discontinuity line. Also, it clearly shows a discontinuity in the gradients normal to the line of material interface for both functions.

It is noted that the unenriched EFG shows an smooth change along the line of discontinuity and is not capable of representing discontinuous gradients and sudden changes in slopes. The amount of oscillations for the ramp function is negligible in contrast to the cubic spline function or unenriched EFG method.

5.3.2. Consolidation of a two-layer partially saturated porous medium in the presence of multiple impermeable discontinuities. As a further step, interaction of weak discontinuity and a set of randomly generated impermeable strong discontinuities, in a nonsaturated porous medium is studied. Discontinuities are assumed to be impermeable with no exchange and coupling of water through its faces, whereas, the singularity in strain fields and pressure gradient at the tip of discontinuity is considered. The water pressure is modeled as a discontinuous field across the discontinuity surfaces by the Heaviside enrichment function (39), while the asymptotic discontinuity-tip enrichment function (41) is used for the tip enriched nodes. In order to capture the weak discontinuity, the ramp function (35) is used. The boundary conditions are similar to previous example and the only difference is the presence of discontinuities. The line of material discontinuity is placed at the mid-height and the width of domain is 0.5m. Distribution of normal and enrichment nodes are shown in Figure 20, which also depicts different sets of discontinuity length and discontinuity tip enrichment nodes. The experimental relations of (44) are exploited for water saturation and permeabilities during the analysis. The problem is solved under the plane strain conditions with the Poisson's ratio of 0.4 and the time step is set to 20s. Contours of water pressure at the background gauss points, depicted in Figure 21, clearly show the effect of enrichment functions. As expected, a discontinuity in water pressure along the discontinuity

DOI: 10.1002/nag

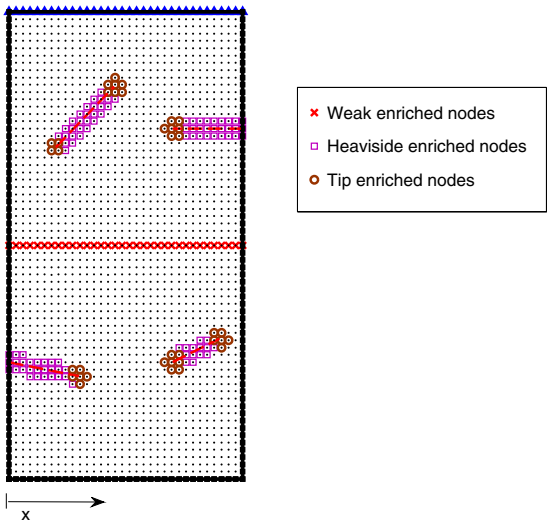

Figure 20. Nodal points for the problem of two-layer partially saturated porous medium with multiple discontinuities.

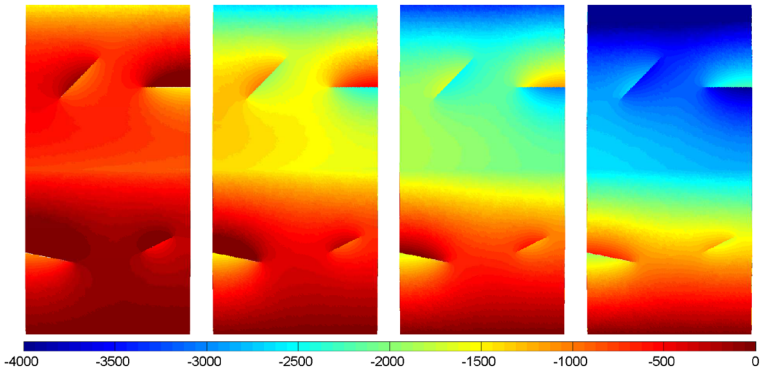

Figure 21. Water pressure distribution (Pa) at times 0, 120, 200, and 1000 s for the problem of partially saturated two-phase porous medium.

length is observed, while a singular pressure gradient at the discontinuity-tip is expected. Variations of water saturations are shown in Figure 22, which similar to water pressure become discontinuous along the discontinuity length. To further discuss the results, a section at the left edge of domain ($x = 0$) is considered. Figure 23 depicts the profiles of displacements and water pressure gradients along this section at a finer scale, which clearly shows the presence of both discontinuity types. It is also observed that as the flow of water continues, water pressure gradients are dissipated and a uniform water pressure gradient along the column height is reached. Contours of vertical strains and pressure gradients computed by a fine background mesh are shown in Figure 24, which better illustrate the presence of discontinuity tip enrichment functions, as relatively large values of derivative fields are generated near the discontinuity tips.

5.4. Three-phase deforming porous media

5.4.1. Consolidation of a partially saturated three-phase deforming porous medium. As the final part of numerical examples, a multiphase partially saturated porous medium is analyzed. The presence of two distinct fluid phases (water and gas) are taken into account by considering both water and gas pressure DOFs.

DOI: 10.1002/nag

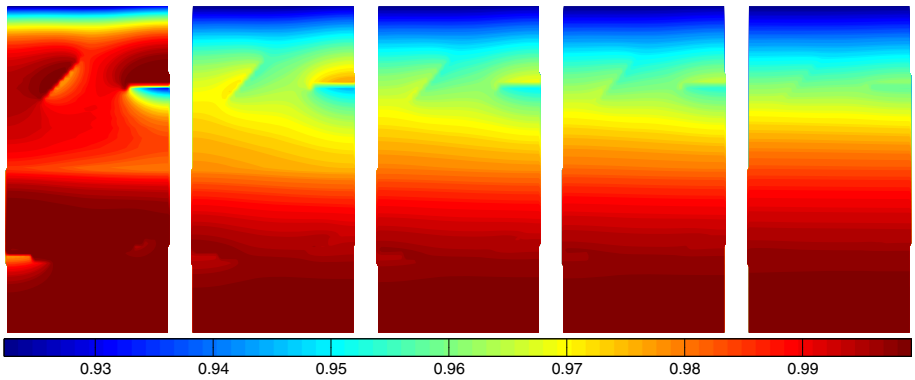

Figure 22. Water saturation values at times 0, 400, 800, 1200, and 4800 s for the problem of partially saturated two-phase porous medium.

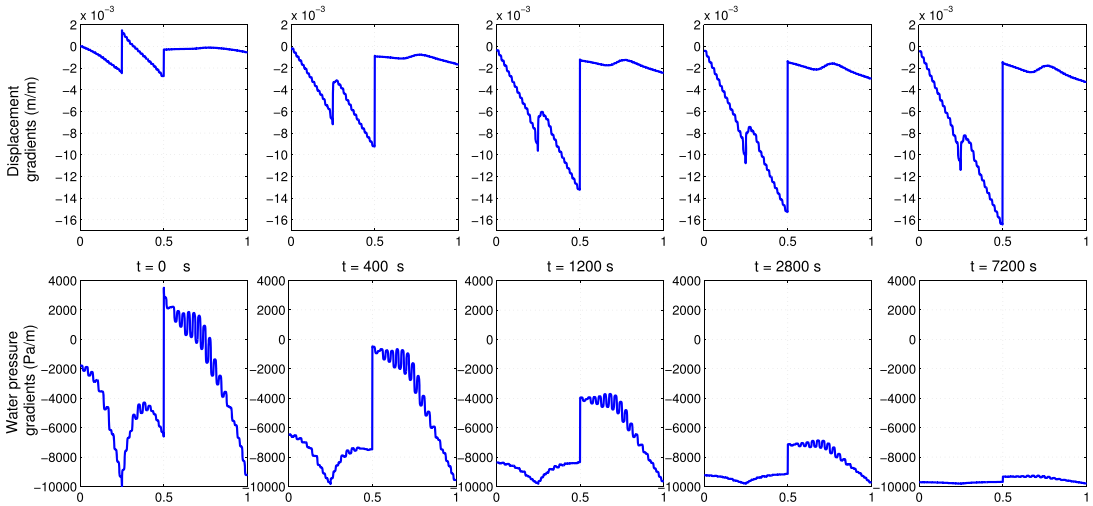

Figure 23. Variations of displacements and water pressure gradients along the section ($x = 0$) for the problem of partially saturated two-phase porous medium.

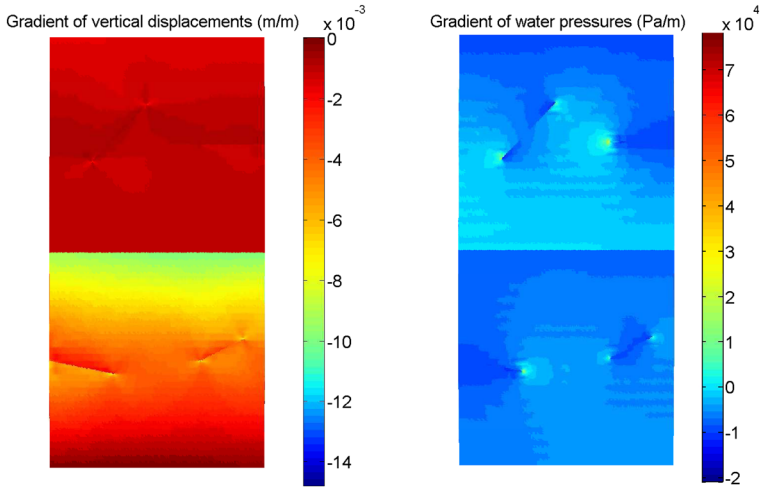

Figure 24. Gradients of displacements and water pressure at time 600 s for the problem of partially saturated two-phase porous media.

DOI: 10.1002/nag

Table III. Material properties for the problem of multilayer partially saturated three-phase porous medium.

Material property	Layer 1	Layer 2	Layer 3	Layer 4
Young modulus (MPa)	1.5	12	3	20.4
Solid density (kg/m^3)	2000	2000	2000	2000
Water density (kg/m^3)	1000	1000	1000	1000
Gas density (kg/m^3)	1.22	1.22	1.22	1.22
Solid bulk modulus (Pa)	0.14×10^{10}	0.14×10^{10}	0.14×10^{10}	0.14×10^{10}
Water bulk modulus (Pa)	0.43×10^{13}	0.43×10^{13}	0.43×10^{13}	0.43×10^{13}
Gas bulk modulus (Pa)	0.1×10^{6}	0.1×10^{6}	0.1×10^{6}	0.1×10^{6}
Water viscosity (Pa.s)	1.0×10^{-3}	1.0×10^{-3}	1.0×10^{-3}	1.0×10^{-3}
Gas viscosity (Pa.s)	1.0×10^{-3}	1.0×10^{-3}	1.0×10^{-3}	1.0×10^{-3}
Intrinsic permeability (m^2)	0.46×10^{-11}	2.07×10^{-11}	0.207×10^{-11}	4.6×10^{-11}
Layer height (m)	0.25	0.25	0.25	0.25
Poisson ratio	0.4	0.4	0.4	0.4
Biot coefficient	1	1	1	1
Porosity	0.2975	0.2975	0.2975	0.2975

This problem was solved by Rahman and Lewis [10] assuming a single layer homogeneous soil by the finite element method, which is often used as a benchmark solution to control the multiphase porous models of an initially nonsaturated state. Recently, Mohammadnejad and Khoei [76] solved the same problem to assess the convergence problems encountered in the extended finite element method because of the presence of blending elements and adopted a set of corrected enrichment functions to recover semi-optimal convergence ratios for four-noded bilinear elements.

The geometry and solid boundary conditions are the same as Liakopolous experiment (solved in Section 5.3.1), which consists of a soil column of 1 m height and 0.1 m width.

The initial state of the problem is arranged so that the soil column remains initially nonsaturated with an initial degree of saturation equal to 0.52 throughout the whole soil column. This implies that initially a uniform water pressure value of -280 KN/m^2 and a uniform gas pressure equal to the atmospheric pressure exist. A uniform downward mechanical load equal to 1000 KN/m^2 is exerted at the top surface and the value of atmospheric pressure is given as 101.8967 kPa. Material properties used in this problem are shown in Table III. The Young's modulus is equal to 6Mpa and other material properties of the medium are similar to layer 1 in the Table III.

At the start of analysis, the water pressure at the surface is instantaneously changed to -420 KN/m^2 due to an environment change and the gas pressure for the top boundary is held constant and equal to the atmospheric pressure during the analysis.

The relative permeability of water phase (k_{rw}), the relative permeability of gas phase (k_{rg}) and the water degree of saturation (S_w) are determined by appropriate experimental relations proposed by Brooks and Corey [77] (as a result, the set of system equations becomes nonlinear),

$$\begin{aligned} S_w &= S_{rw} + (1 - S_{rw}) \left(\frac{p_b}{p_c} \right)^{\lambda}, \quad S_e = \frac{S_w - S_{rw}}{1 - S_{rw}} \\ k_{rw} &= S_e^{\frac{2+3\lambda}{\lambda}} \\ k_{ra} &= (1 - S_e)^2 \left(1 - S_e^{\frac{2+\lambda}{\lambda}} \right) \end{aligned} \tag{45}$$

with:

$$S_{rw} = 0.3966 \qquad p_b = 225 \frac{kN}{m^2} \qquad \lambda = 3$$

Figure 25 illustrates variations of vertical displacement and water saturation in time for different distances from the column top, whereas Figure 26 depicts the distribution of water and gas pressures along the column height for different time steps. Clearly, the results of the present EFG formulation

DOI: 10.1002/nag

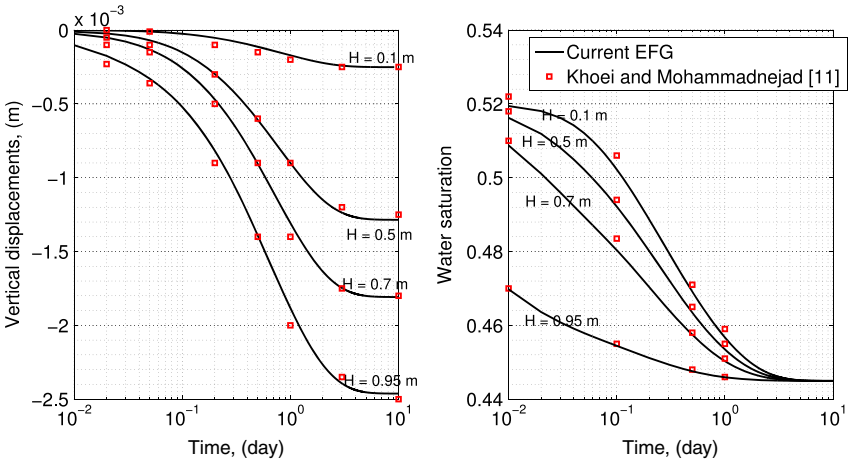

Figure 25. Vertical displacements and water saturation for the problem of three-phase partially saturated single-layer porous medium.

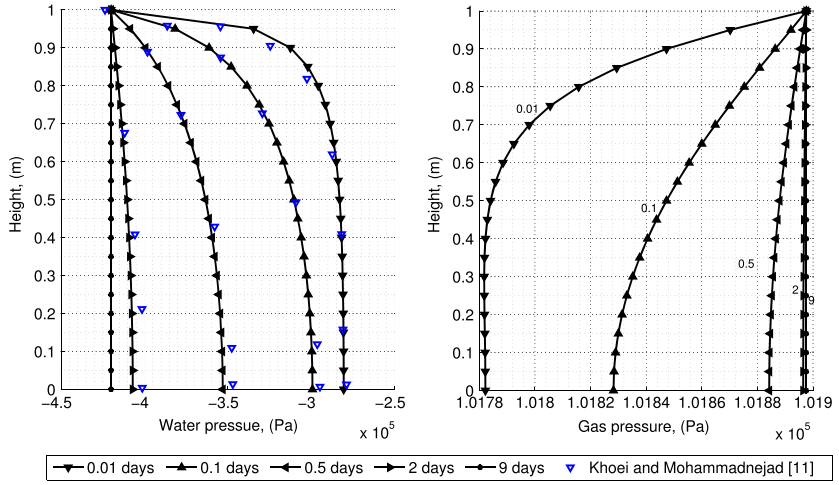

Figure 26. Water and gas pressures for the problem of three-phase partially saturated single-layer porous medium.

are in complete agreement with the reference results reported by Rahman and Lewis[10] and Khoei and Mohammadnejad [11].

5.4.2. Consolidation of a partially saturated three-phase deforming porous medium in the presence of weak discontinuities. Now, the same problem is considered in the presence of material discontinuities. The soil column is constructed of four equally spaced sublayers with material discontinuity lines at heights 0.25, 0.5 and 0.75 with respect to the base of column with different Young's modules and permeabilities of gas and water phases, which results in discontinuity in gradient of solid displacements, and water and gas pressures normal to the lines of discontinuities. A set of uniform 5×33 nodal points are used.

The value of the intrinsic permeabilities are assumed as: $k_1 = 0.46 \times 10^{-11}(m^2)$, $k_2 = 4.5k_1$, $k_3 = 0.45k_1$ and $k_4 = 10k_1$; with large discrepancies so that the material interfaces become apparent in the pressure fields.

The material properties of layers are defined in Table III. As shown in Figure 27, water and gas pressure dissipation patterns change dramatically for the new material composition as different material properties are involved. It is apparent that because of large permeability of the top layer (ten times

DOI: 10.1002/nag

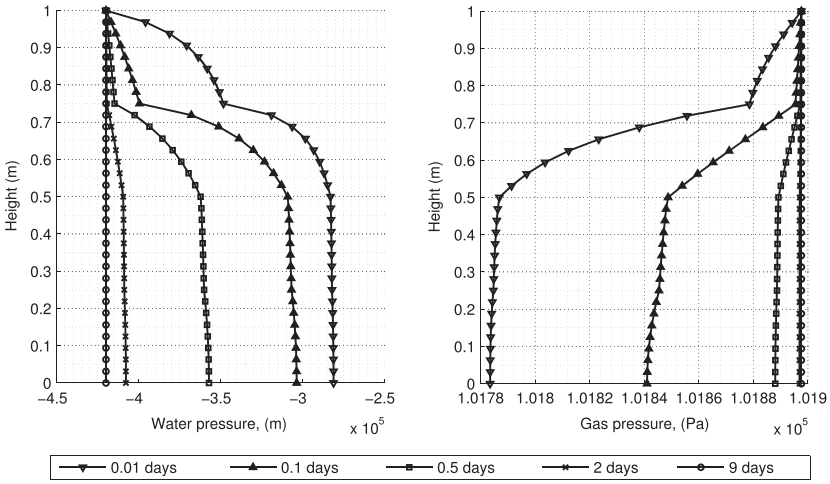

Figure 27. Water and gas pressures for the problem of three-phase partially saturated multilayer porous medium.

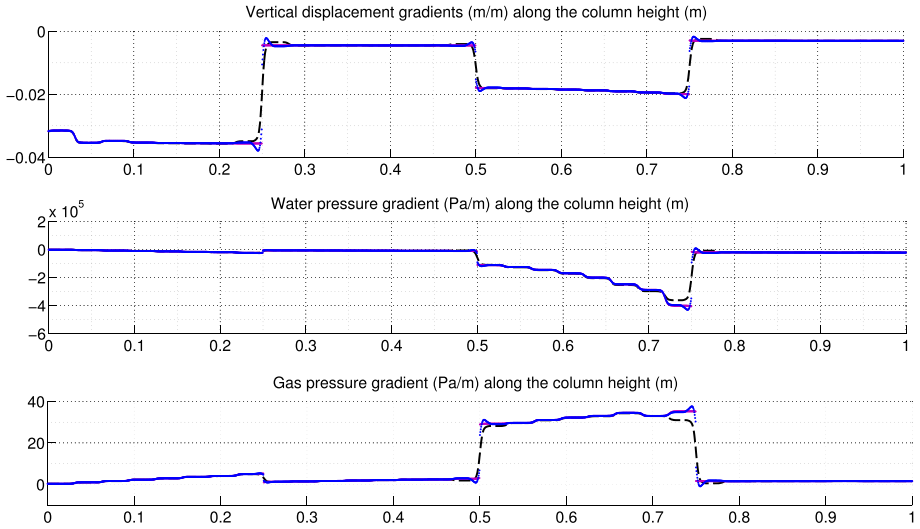

Figure 28. Variations of gradients along the column height at time $t = 0.5$ days for the pure EFG, enriched EFG by the cubic spline function and enriched EFG by the ramp function.

of the lowest layers), water and gas pressures are dissipated faster. The final state is reached after 9 days of analysis in which the results for multilayer and single layer cases are equivalent to the initially applied boundary pressures.

Figure 28 shows the results of vertical strains and vertical gradients of fluid phases, analyzed by the developed enriched EFG formulation for the case of multilayer multiphase porous media. Although the displacement and pressure fields are continuous at the lines of discontinuity, a discontinuity of the form of the Heaviside function is present in the solution for the first derivative fields. The proposed enrichment algorithm generates a continuous distribution for the field variables across the line of discontinuity while it is capable of reproducing a jump in its first derivatives. Only minor oscillations are present in the solution, which can be neglected without the loss of accuracy. Figure 29 illustrates the values of gradients in a finer scale, which shows that the ramp function is a more suitable approach to model weak discontinuities of material interfaces. Despite the oscillatory results, the cubic spline function can also capture the material discontinuity, and it is preferred to unenriched EFG solutions.

DOI: 10.1002/nag

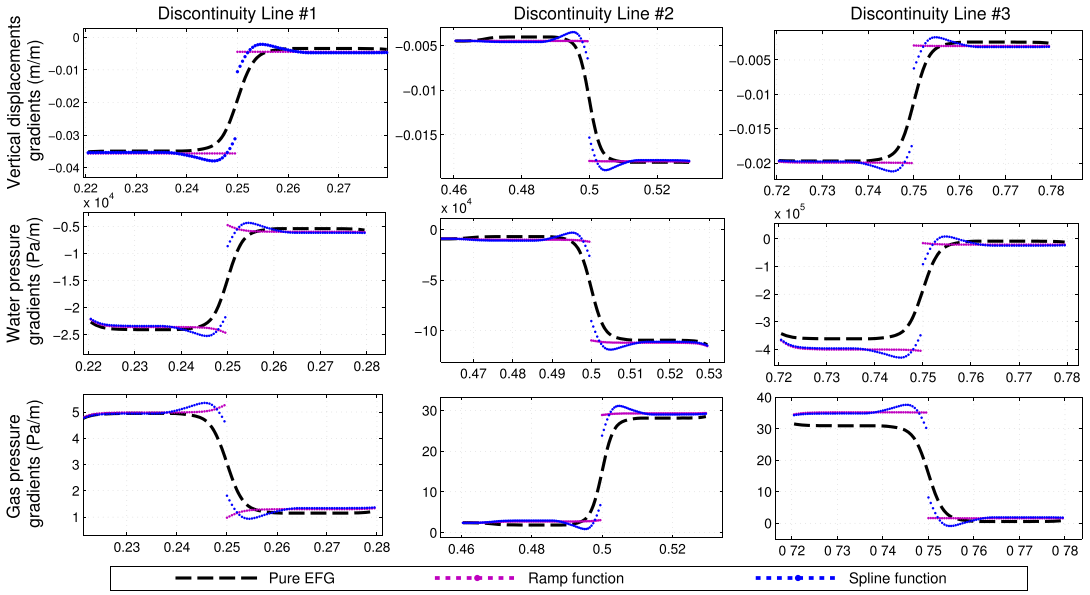

Figure 29. Magnified values of gradients along the column height at time 0.5 days for the unenriched EFG, enriched EFG by the cubic spline function, and enriched EFG by the ramp function.

6. CONCLUSION

An enriched mesh-free EFG formulation for fully coupled porous systems was proposed in this study to handle weak and strong discontinuities throughout the domain. This work is presumed to be the first attempt to analysis of discontinuities in porous media using the enriched mesh-free method. Adopting extrinsically enriched MLS approximations for solid displacement, water pressure and gas pressure, the discretized set of equations were derived. Due to lack of Kronecker delta property of MLS shape functions, the constrained weak form of equations were written in the context of the Lagrangian approach. A nonlinear iterative solution procedure was implemented to solve the nonlinear constrained fully coupled system of equations in the partially saturated state. A set of examples, including one-dimensional saturated consolidation, two dimensional saturated and partially saturated states with assumptions of passive and active gas pressures, were numerically discussed and the derivative fields were computed as a multiplication of discontinuous Heaviside function. It was shown that the proposed enrichment strategy could eliminate the expecting oscillations around the material discontinuities encountered in unenriched and constrained mesh-free methods. The interaction of multiple impermeable discontinuities with material interfaces were assessed and the proposed enrichment strategies for weak and strong discontinuities were verified by various problems in poro-elasticity.

APPENDIX A

The final forms of the discretized matrices/vectors of the governing equation (22) can be written as:

$$\mathbf{K} = \int_{\Omega} \mathbf{B}_{\mathbf{u}}^{\mathrm{T}} \mathbf{D} \mathbf{B}_{\mathbf{u}}, d\Omega \qquad \mathbf{K} = \begin{bmatrix} \mathbf{K}^{\mathbf{uu}} & \mathbf{K}^{\mathbf{ua}} & \mathbf{K}^{\mathbf{ub}} \\ \mathbf{K}^{\mathbf{au}} & \mathbf{K}^{\mathbf{aa}} & \mathbf{K}^{\mathbf{ab}} \\ \mathbf{K}^{\mathbf{bu}} & \mathbf{K}^{\mathbf{ba}} & \mathbf{K}^{\mathbf{bb}} \end{bmatrix} \tag{A.1}$$

$$\mathbf{C}_{\mathbf{sw}} = \int_{\Omega} \mathbf{B}_{\mathbf{u}}^{\mathrm{T}} \alpha S_w \mathbf{m} \mathbf{N}_{\mathbf{p_w}} d\Omega, \qquad \mathbf{C}_{\mathbf{sw}} = \begin{bmatrix} \mathbf{C}_{\mathbf{sw}}^{\mathbf{up_w}} & \mathbf{C}_{\mathbf{sw}}^{\mathbf{uc}} & \mathbf{C}_{\mathbf{sw}}^{\mathbf{ud}} \\ \mathbf{C}_{\mathbf{sw}}^{\mathbf{ap_w}} & \mathbf{C}_{\mathbf{sw}}^{\mathbf{ac}} & \mathbf{C}_{\mathbf{sw}}^{\mathbf{ad}} \\ \mathbf{C}_{\mathbf{sw}}^{\mathbf{bp_w}} & \mathbf{C}_{\mathbf{sw}}^{\mathbf{bc}} & \mathbf{C}_{\mathbf{sw}}^{\mathbf{bd}} \end{bmatrix} \tag{A.2}$$

DOI: 10.1002/nag

$$\mathbf{C_{sa}} = \int_{\Omega} \mathbf{B_u^T} \alpha (1 - S_w) \mathbf{m} \mathbf{N_{p_a}} d\Omega, \qquad \mathbf{C_{sa}} = \begin{bmatrix} \mathbf{C_{sa}}^{\mathbf{up_a}} & \mathbf{C_{sa}}^{\mathbf{uc}} \\ \mathbf{C_{sa}}^{\mathbf{ap_a}} & \mathbf{C_{sa}}^{\mathbf{ac}} \\ \mathbf{C_{sa}}^{\mathbf{bp_a}} & \mathbf{C_{sa}}^{\mathbf{bc}} \end{bmatrix} \tag{A.3}$$

$$\mathbf{C_{ws}} = \int_{\Omega} \mathbf{N_{p_w}^T} \alpha S_w \mathbf{m^T} \mathbf{B_u} d\Omega, \qquad \mathbf{C_{ws}} = \begin{bmatrix} \mathbf{C_{ws}}^{\mathbf{p_w u}} & \mathbf{C_{ws}}^{\mathbf{p_w a}} & \mathbf{C_{ws}}^{\mathbf{p_w b}} \\ \mathbf{C_{ws}}^{\mathbf{cu}} & \mathbf{C_{ws}}^{\mathbf{ca}} & \mathbf{C_{ws}}^{\mathbf{cb}} \\ \mathbf{C_{ws}}^{\mathbf{du}} & \mathbf{C_{ws}}^{\mathbf{da}} & \mathbf{C_{ws}}^{\mathbf{db}} \end{bmatrix} \tag{A.4}$$

$$\mathbf{P_{ww}} = \int_{\Omega} \mathbf{N_{p_w}^T} (Q_{ww}) \mathbf{N_{p_w}} d\Omega, \qquad \mathbf{P_{ww}} = \begin{bmatrix} \mathbf{P_{ww}}^{\mathbf{p_w p_w}} & \mathbf{P_{ww}}^{\mathbf{p_w c}} & \mathbf{P_{ww}}^{\mathbf{p_w d}} \\ \mathbf{P_{ww}}^{\mathbf{cp_w}} & \mathbf{P_{ww}}^{\mathbf{cc}} & \mathbf{P_{ww}}^{\mathbf{cd}} \\ \mathbf{P_{ww}}^{\mathbf{dp_w}} & \mathbf{P_{ww}}^{\mathbf{dc}} & \mathbf{P_{ww}}^{\mathbf{dd}} \end{bmatrix} \tag{A.5}$$

$$\mathbf{C_{wa}} = \int_{\Omega} \mathbf{N_{p_w}^T} (Q_{wa}) \mathbf{N_{p_a}} d\Omega, \qquad \mathbf{C_{wa}} = \begin{bmatrix} \mathbf{C_{wa}}^{\mathbf{p_w p_a}} & \mathbf{C_{wa}}^{\mathbf{p_w c}} \\ \mathbf{C_{wa}}^{\mathbf{cp_a}} & \mathbf{C_{wa}}^{\mathbf{cc}} \\ \mathbf{C_{wa}}^{\mathbf{dp_a}} & \mathbf{C_{wa}}^{\mathbf{dc}} \end{bmatrix} \tag{A.6}$$

$$\mathbf{H_{ww}} = \int_{\Omega} \left(\mathbf{L_{pw}} \mathbf{N_{p_w}}\right)^{\mathbf{T}} \mathbf{k_w} \left(\mathbf{L_{pw}} \mathbf{N_{p_w}}\right) d\Omega, \qquad \mathbf{H_{ww}} = \begin{bmatrix} \mathbf{H_{ww}}^{\mathbf{p_w p_w}} & \mathbf{H_{ww}}^{\mathbf{p_w c}} & \mathbf{H_{ww}}^{\mathbf{p_w d}} \\ \mathbf{H_{ww}}^{\mathbf{cp_w}} & \mathbf{H_{ww}}^{\mathbf{cc}} & \mathbf{H_{ww}}^{\mathbf{cd}} \\ \mathbf{H_{ww}}^{\mathbf{dp_w}} & \mathbf{H_{ww}}^{\mathbf{dc}} & \mathbf{H_{ww}}^{\mathbf{dd}} \end{bmatrix} \tag{A.7}$$

$$\mathbf{C_{as}} = \int_{\Omega} \mathbf{N_{p_a}^T} \alpha (1 - S_w) \mathbf{m^T} \mathbf{B_u} d\Omega, \qquad \mathbf{C_{as}} = \begin{bmatrix} \mathbf{C_{as}}^{\mathbf{p_a u}} & \mathbf{C_{as}}^{\mathbf{p_a a}} & \mathbf{C_{as}}^{\mathbf{p_a b}} \\ \mathbf{C_{as}}^{\mathbf{cu}} & \mathbf{C_{as}}^{\mathbf{ca}} & \mathbf{C_{as}}^{\mathbf{cb}} \end{bmatrix} \tag{A.8}$$

$$\mathbf{P_{aa}} = \int_{\Omega} \mathbf{N_{p_a}^T} (Q_{aa}) \mathbf{N_{p_a}} d\Omega, \qquad \mathbf{P_{aa}} = \begin{bmatrix} \mathbf{P_{aa}}^{\mathbf{p_a p_a}} & \mathbf{P_{aa}}^{\mathbf{p_a c}} \\ \mathbf{P_{aa}}^{\mathbf{cp_a}} & \mathbf{P_{aa}}^{\mathbf{cc}} \end{bmatrix} \tag{A.9}$$

$$\mathbf{C_{aw}} = \int_{\Omega} \mathbf{N_{p_a}^T} (Q_{aw}) \mathbf{N_{p_w}} d\Omega, \qquad \mathbf{C_{aw}} = \begin{bmatrix} \mathbf{C_{aw}}^{\mathbf{p_a p_w}} & \mathbf{C_{aw}}^{\mathbf{p_a c}} & \mathbf{C_{aw}}^{\mathbf{p_a d}} \\ \mathbf{C_{aw}}^{\mathbf{cp_w}} & \mathbf{C_{aw}}^{\mathbf{cc}} & \mathbf{C_{aw}}^{\mathbf{cd}} \end{bmatrix} \tag{A.10}$$

$$\mathbf{H_{aa}} = \int_{\Omega} \left(\mathbf{L_{pa}} \mathbf{N_{p_a}}\right)^{\mathbf{T}} \mathbf{k_a} \left(\mathbf{L_{pa}} \mathbf{N_{p_a}}\right) d\Omega, \qquad \mathbf{H_{aa}} = \begin{bmatrix} \mathbf{H_{aa}}^{\mathbf{p_a p_a}} & \mathbf{H_{aa}}^{\mathbf{p_a c}} \\ \mathbf{H_{aa}}^{\mathbf{cp_a}} & \mathbf{H_{aa}}^{\mathbf{cc}} \end{bmatrix} \tag{A.11}$$

$$\mathbf{F_u} = \int_{\Omega} \mathbf{N_u^T} \rho \boldsymbol{b} d\Omega + \int_{\Gamma_u} \mathbf{N_u^T} \rho \bar{\boldsymbol{t}} \, d\Gamma_u \tag{A.12}$$

$$\mathbf{F_w} = \int_{\Omega} \left(\mathbf{L_{pw}} \mathbf{N_{p_w}}\right)^{\mathbf{T}} \frac{\boldsymbol{k} k_{rw}}{\mu_w} \rho_w \mathbf{b} d\Omega - \int_{\Gamma_{pw}} \mathbf{N_{p_w}^T} \frac{\bar{q_w}}{\rho_w} \, d\Gamma_{pw} \tag{A.13}$$

$$\mathbf{F_a} = \int_{\Omega} \left(\mathbf{L_{pa}} \mathbf{N_{p_a}}\right)^{\mathbf{T}} \frac{\boldsymbol{k} k_{ra}}{\mu_a} \rho_a \mathbf{b} d\Omega - \int_{\Gamma_{pa}} \mathbf{N_{p_a}^T} \frac{\bar{q_a}}{\rho_a} \, d\Gamma_{pa} \tag{A.14}$$

and

$$\begin{aligned} \mathbf{B_u} &= \begin{bmatrix} \mathbf{B^{std}} & \mathbf{B_u^a} & \mathbf{B_u^b} \end{bmatrix} \\ \mathbf{N_u} &= \begin{bmatrix} \mathbf{N_u^{std}} & \mathbf{N_u^a} & \mathbf{N_u^b} \end{bmatrix} \\ \mathbf{N_{pw}} &= \begin{bmatrix} \mathbf{N_{pw}^{std}} & \mathbf{N_{pw}^c} & \mathbf{N_{pw}^d} \end{bmatrix} \\ \mathbf{N_{pa}} &= \begin{bmatrix} \mathbf{N_{pa}^{std}} & \mathbf{N_{pa}^c} \end{bmatrix} \end{aligned} \tag{A.15}$$

where the following notations are used for different enrichment types A.1,

DOI: 10.1002/nag

Table A.1. Notations for different enrichment types.

Field variable	Standard	Heaviside or ψ(weak)	Tip
Displacement	u	a	b
Water pressure	p_w	c	d
Gas pressure	p_a	c	–

and the nonlinear terms are elaborated as follows:

$$
\begin{aligned}
Q_{ww} &= \left[S_w \frac{\alpha - n}{K_s} . \left(S_w + \frac{\partial S_w}{\partial p_c} . p_c \right) + \frac{n . S_w}{K_w} - n . \frac{\partial S_w}{\partial p_c} \right] \\
Q_{wa} &= \left[S_w \frac{\alpha - n}{K_s} . \left(1 - S_w - \frac{\partial S_w}{\partial p_c} . p_c \right) + n . \frac{\partial S_w}{\partial p_c} \right] \\
Q_{aa} &= \left[(1 - S_w) \frac{\alpha - n}{K_s} . \left(1 - S_w - \frac{\partial S_w}{\partial p_c} . p_c \right) + \frac{n . (1 - S_w)}{K_w} - n . \frac{\partial S_w}{\partial p_c} \right] \\
Q_{aw} &= \left[(1 - S_w) \frac{\alpha - n}{K_s} . \left(S_w + \frac{\partial S_w}{\partial p_c} . p_c \right) + n . \frac{\partial S_w}{\partial p_c} \right]
\end{aligned}
\tag{A.16}
$$

Because all these terms are functions of the water pressure, so the total system of equations becomes non linear, which requires an appropriate nonlinear algorithm to solve the fully coupled multiphase system of equations.

ACKNOWLEDGEMENTS

The authors wish to acknowledge the technical support of the High Performance Computing Lab, University of Tehran. Also, the support of Iran National Science Foundation is gratefully appreciated.

REFERENCES

1. Terzaghi K. *Theoretical Soil Mechanics*. Wiley: New York, 1943.
2. Biot MA. General theory of three-dimensional consolidation. *Journal of Applied Physics* 1941; **12**:155–164.
3. Hassanizadeh M, Gray WG. General conservation equations for multi-phase systems: 1. Averaging procedure. *Advances in Water Resources* 1979; **2**:131–144.
4. Hassanizadeh M, Gray WG. General conservation equations for multi-phase systems: 2. Mass, momenta, energy, and entropy equations. *Advances in Water Resources* 1979; **2**:191–203.
5. Lewis RW, Schrefler BA. *The Finite Element Method in the Static and Dynamic Deformation and Consolidation of Porous Media*. Wiley: Chichester, 1998.
6. Schrefler BA, Xiaoyong Z. A fully coupled model for water flow and airflow in deformable porous media. *Water Resources Research* 1993; **29**:155–167.
7. Schrefler B, Scotta R. A fully coupled dynamic model for two-phase fluid flow in deformable porous media. *Computer Methods in Applied Mechanics and Engineering* 2001; **190**:3223–3246.
8. Gawin D, Schrefler B. Thermo-hydro-mechanical analysis of partially saturated porous materials. *Engineering Computations* 1996; **13**:113–143.
9. Schrefler B, Zhan X, Simoni L. A Coupled Model for water flow, airflow and heat flow in deformable porous media. *International Journal of Numerical Methods for Heat and Fluid Flow* 1995; **5**:531–547.
10. Rahman NA, Lewis RW. Finite element modeling of multiphase immiscible flow in deforming porous media for subsurface systems. *Computers and Geotechnics* 1999; **24**:41–63.
11. Khoei AR, Mohammadnejad T. Numerical modeling of multiphase fluid flow in deforming porous media: A comparison between two- and three-phase models for seismic analysis of earth and rockfill dams. *Computers and Geotechnics* 2011; **38**:142–166.
12. Kardani M, Nazem M, Sheng D, Carter JP. Large deformation analysis of geomechanics problems by a combined rh-adaptive finite element method. *Computers and Geotechnics* 2013; **49**:90–99.
13. Khoshghalb A. Meshfree analysis of unsaturated porous media including hydraulic hystersis and large deformation. *Ph.D. Thesis*, The University of New South Wales, Sydney, Australia, 2011.
14. Carpinteri A, Nazem M, Colombo G. Numerical analysis of catastrophic softening behaviour (snap-back instability). *Computers and Structures* 1989; **31**:607–636.

DOI: 10.1002/nag

15. Lamb AR, Gorman GJ, Elsworth D. A fracture mapping and extended finite element scheme for coupled deformation and fluid flow in fractured porous media. *International Journal for Numerical and Analytical Methods in Geomechanics* 2013; **37**:2916–2936.
16. Belytschko T, Lu YY, Gu L. International Journal for Numerical Methods in Engineering 1994; **37**:229–256.
17. Liu GR. *Mesh Free Methods: Moving Beyond the Finite Element Method*. CRC Press: Boca Raton, 2003.
18. Liu GR, Gu L. *An Introduction to Meshfree Methods and Their Programming*. Springer: Dordrecht, The Netherlands, 2005.
19. Belytschko T, Krongauz Y, Organ D, Fleming M, Krysl P. Meshless method: an overview and recent developments. *Computer Methods in Applied Mechanics and Engineering* 1996; **139**:3–47.
20. Ghorashi SH, Mohammadi S, Sabbagh-yazdi SR. Orthotropic enriched element free Galerkin method for fracture analysis of composites. *Engineering Fracture Mechanics* 2011; **78**:1906–1927.
21. Modaressi H, Auber P. Element-free galerkin method for deforming multiphase porous media. *International Journal for Numerical Methods in Engineering* 2002; **39**:1557–1573.
22. Wang JG, Liu GR, Lin P. Numerical analysis of Biot's consolidation process by radial point interpolation method. *International Journal of Solid and Structures* 2002; **39**:1557–1573.
23. Samimi S, Pak A. Three-dimensional simulation of fully coupled hydro-mechanical behavior of saturated porous media using Element Free Galerkin (EFG) method. *Computers and Geotechnics* 2012; **46**:75–83.
24. Khoshghalb A, Khalili N. A stable meshfree method for fully coupled flow-deformation analysis of saturated porous media. *Computers and Geotechnics* 2012; **37**:789–795.
25. Khoshghalb A, Khalili N. A meshfree method for fully coupled analysis of flow and deformation in unsaturated porous media. *International Journal for Numerical and Analytical Methods in Geomechanics* 2012; **37**:716–743.
26. Hua L. Stable element-free Galerkin solution procedures for the coupled soil-pore fluid problem. *International Journal for Numerical Methods in Engineering* 2010; **86**:1000–1026.
27. Chen JS, Wu CT, Chi L, Huck F. A mesh-free method for geotechnical materials. *Journal of Engineering Mechanics (ASCE)* 2001; **127**:440–449.
28. Nogami T, Wang W, Wang JG. Numerical method for consolidation analysis of clumpy clay fillings with meshless method. *Soils and Foundations* 2004; **44**(1):125–42.
29. Oliaei MN, Soga K, Pak A. Some numerical issues using element-free Galerkin mesh-less method for coupled hydro-mechanical problems. *International Journal for Numerical and Analtical Methods in Geomechics* 2009; **33**:915–38.
30. Wang JG, Liu GR, Wu YG. A point interpolation method for simulating dissipation process of consolidation. *Computer Methods in Applied Mechanics and Engineering* 2001; **190**:5907–5922.
31. Strouboulis T, Copps K, Babuska I. The generalized finite element method. *Computer Methods in Applied Mechanics and Engineering* 2001; **190**:4081–4193.
32. Melenk JM, Babuska I. The partition of unity finite element method. *Computer Methods in Applied Mechanics and Engineering* 1996; **39**:289–314.
33. Moes N, Dolbow J, Belytschko T. A finite element method for crack growth without remeshing. *International Journal for Numerical Methods in Engineering* 1999; **46**:131–150.
34. Belytschko T, Black T. Elastic crack growth in finite element method: Basic theory and applications. *Computer Methods in Applied Mechanics and Engineering* 1999; **139**:289–314.
35. Mohammadi S. *Extended Finite Element Method.* Blackwell: Oxford, 2007.
36. Mohammadi S. *XFEM Fracture Analysis of Composites*. Wiley: Chichester, 2012.
37. Sukumar N, Chopp DL, Moes N, Belytschko T. Modeling holes and inclusions by level sets in the extended finite element method. *Computer Methods in Applied Mechanics and Engineering* 2001; **190**:6183–6200.
38. Chessa J, Wang H, Belytschko T. On the construction of blending elements for local partition of unity enriched finite elements. *International Journal for Numerical Methods in Engineering* 2003; **57**:1015–1038.
39. Moes N, Cloirec M, Cartraud P, Remacle JF. A computational approach to handle complex microstructure geometries. *Computer Methods in Applied Mechanics and Engineering* 2003; **192**:3163–3177.
40. Ji H, Dolbow JE. A computational approach to handle complex microstructure geometries. *Computer Methods in Applied Mechanics and Engineering* 2003; **192**:3163–3177.
41. Esna Ashari S, Mohammadi S. Delamination analysis of composites by new orthotropic bimaterial extended finite element method. *International Journal for Numerical Methods is Engineering* 2011; **86**:1507–1543.
42. Rethore J, de Borst R, Abellan MA. A two-scale approach for fluid flow in fractured porous media. *International Journal for Numerical Methods in Engineering* 2007; **71**:780–800.
43. Rethore J, de Borst R, Abellan MA. A two-scale approach for fluid flow in an non-saturated porous medium with cohesive cracks. *Computational Mechanics* 2008; **42**:227–238.
44. Mohammadnejad T, Khoei AR. Hydro-mechanical modeling of cohesive crack propagation in multiphase porous media using the extended finite element method. *International Journal for Numerical and Analytical Methods in Geomechanics* 2012; **37**:1247–1279.
45. Irzal F, Remmers JC, Huyghe JM, de Borst R. A large deformation formulation for fluid flow in progressively fracturing porous material. *Computer Methods in Applied Mechanics and Engineering* 2013; **256**:29–37.
46. Khoei AR, Moallemi S, Haghighat E. Thermo-hydro-mechanical modeling of impermeable discontinuity in saturated porous media with X-FEM technique. *Engineering Fracture Mechanics* 2012; **96**:701–723.

DOI: 10.1002/nag

47. Rabczuk T, Bordas S, Zi G. A three-dimensional meshfree method for continuous multiplecrack initiation, nucleation and propagation in statics and dynamics. *Computational Mechanics* 2007; **40**(3):473–495.
48. Rabczuk T, Belytschko T. A three dimensional large deformation meshfree method for arbitrary evolving cracks. *Computer Methods in Applied Mechanics and Engineering* 2007; **196**(29-30):2777–2799.
49. Rabczuk T, Belytschko T. Cracking particles: a simplified meshfree method for arbitrary evolving cracks. *International Journal for Numerical Methods in Engineering* 2004; **61**(13):2316–2343.
50. Rabczuk T, Areias PMA, Belytschko T. A simplified meshfree method for shear bands with cohesive surfaces. *International Journal for Numerical Methods in Engineering* 2007; **69**(5):993–1021.
51. Rabczuk T, Areias PMA. A new approach for modelling slip lines in geological materials with cohesive models. *International Journal for Numerical and Analytical Methods in Engineering* 2006; **30**(11):1159–1172.
52. Rabczuk T, Areias PMA. A meshfree thin shell for arbitrary evolving cracks based on an external enrichment. *CMES-Computer Modeling in Engineering and Sciences* 2006; **16**(2):115–130.
53. Rabczuk T, Areias PMA, Belytschko T. A meshfree thin shell method for nonlinear dynamic fracture. *International Journal for Numerical Methods in Engineering* 2007; **72**(5):524–548.
54. Rabczuk T, Gracie R, Song JH, Belytschko T. Immersed particle method for fluid-structure interaction. *International Journal for Numerical Methods in Engineering* 2010; **81**(1):48–71.
55. Ventura G, Xu JX, Belytschko T. A vector level set method and new discontinuity approximations for crack growth by EFG. *International Journal for Numerical Methods in Engineering* 2002; **54**:923–944.
56. Rabczuk T, Zi G. A meshfree method based on the local partition of unity for cohesive cracks. *Computational Mechanics* 2007; **39**:743–760.
57. Rabczuk T, Zi G, Bordas S, Nguyen-Xuan H. A geometrically non-linear three dimensional cohesive crack method for reinforced concrete structures. *Engineering Fracture Mechanics* 2008; **75**(16):4740–4758.
58. Bordas S, Rabczuk T, Zi G. Three-dimensional crack initiation, propagation, branching and junction in non-linear materials by extrinsic discontinuous enrichment of meshfree methods without asymptotic enrichment. *Engineering Fracture Mechanics* 2008; **75**(5):943–960.
59. Krongauz Y, Belytschko T. EFG approximation with discontinuous derivatives. *International Journal for Numerical Methods in Engineering* 1998; **41**:1215–1233.
60. Cordes LW, Moran B. Treatment of material discontinuity in the Element-Free Galerkin method. *Computer Methods in Applied Mechanics and Engineering* 1996; **139**:75–89.
61. Carpinteri A, Ferro G, Ventura G. An augmented lagrangian approach to material discontinuities in meshless methods. *Computational Mechanics* 2006; **37**:207–220.
62. Ventura G. An augmented Lagrangian approach to essential boundary conditions in meshless methods. *International Journal for Numerical Methods in Engineering* 2002; **53**:825–842.
63. Nguyen VP, Rabczuk T, Bordas S, Duflot M. Meshless methods: A review and computer implementation aspects. *Mathematics and Computers in Simulation* 2008; **79**:763–813.
64. Williams ML. On the stress distribution at the base of a stationary crack. *Journal of Applied Mechanics* 1957; **24**:109–114.
65. Yosibash Z. Numerical thermo-elastic analysis of singularities in two-dimensions. *International Journal of Fracture* 1995; **74**:341–361.
66. Larsson J, Larsson R. Finite-element analysis of localization of deformation and fluid pressure in an elastoplastic porous medium. *International Journal of Solids and Structures* 2000; **37**(48-50):7231–7257.
67. Nikbakht M. Automated Solution of Partial Differential Equations with Discontinuities using the Partition of Unity Method. *Ph.D. Thesis*, Delft University of Technology, 2006.
68. Lee PKK, Xie KH, Cheung YK. A Study on one-dimensional consolidation of layered systems. *International Journal for numerical methods in Geomechnics* 1992; **16**:815–831.
69. Schiffman RL, Stein JR. One-dimensional consolidation of layered systems. *Journal of the Soil Mechanics and Foundations Division, Proceedings of the ASCE*; **96**:1499–1504.
70. Rabczuk T, Belytschko T, Xiao SP. Stable particle methods based on Lagrangian kernels. *Computer Methods in Applied Mechanics and Engineering* 2004; **193**(12-14):1035–1063.
71. Booker JR, Small JC. International Journal for Numerical and Analytical Methods in Geomechanics 1987; **11**:363–380.
72. Booker JR, Small JC. Finite layer analysis of consolidation I. *International Journal for Numerical and Analytical Methods in Geomechanics* 1982; **6**:151–171.
73. Gibson RE, Schiffman RL. Plane Strain and Axillary symmetric consolidation of a clay layer on a smooth impervious base. *Quarterly Journal of Mechanics and Applied Mathematics* 1970; **23**(4):505–520.
74. Liakopoulos AC. Transient flow through unsaturated porous media. *Ph.D Thesis*, University of California, Berkeley, CA, 1965.
75. Gawin D, Baggio P, Schrefler B. Coupled heat, water and gas flow in deformable porous media. *International Journal for Numerical Methods in Fluids* 1995; **20**:969–987.
76. Mohammadnejad T, Khoei AR. An extended finite element method for fluid flow in partially saturated porous media with weak discontinuities; the convergence analysis of local enrichment strategies. *Computational Mechanics* 2013; **51**:327–345.
77. Brooks RN, Corey AT. Properties of porous media affecting fluid flow. *Journal of Irrigation and Drainage Engineering (ASCE)* 1966; **92**:61–68.

DOI: 10.1002/nag